



HAL
open science

PHANGS CO Kinematics: Disk Orientations and Rotation Curves at 150 pc Resolution

Yoon-Hyun Ryu, Andrzej Udalski, Jennifer C. Yee, Matthew T. Penny, Weicheng Zang, Michael D. Albrow, Sun-Ju Chung, Andrew Gould, Cheongho Han, Kyu-Ha Hwang, et al.

► **To cite this version:**

Yoon-Hyun Ryu, Andrzej Udalski, Jennifer C. Yee, Matthew T. Penny, Weicheng Zang, et al.. PHANGS CO Kinematics: Disk Orientations and Rotation Curves at 150 pc Resolution. *The Astrophysical Journal*, 2020, 10.3847/1538-4357/ab9953 . insu-03673120

HAL Id: insu-03673120

<https://insu.hal.science/insu-03673120>

Submitted on 27 Mar 2024

HAL is a multi-disciplinary open access archive for the deposit and dissemination of scientific research documents, whether they are published or not. The documents may come from teaching and research institutions in France or abroad, or from public or private research centers.

L'archive ouverte pluridisciplinaire **HAL**, est destinée au dépôt et à la diffusion de documents scientifiques de niveau recherche, publiés ou non, émanant des établissements d'enseignement et de recherche français ou étrangers, des laboratoires publics ou privés.



PHANGS CO Kinematics: Disk Orientations and Rotation Curves at 150 pc Resolution

Philipp Lang¹, Sharon E. Meidt², Erik Rosolowsky³, Joseph Nofech³, Eva Schinnerer¹, Adam K. Leroy⁴, Eric Emsellem^{5,6}, Ismael Pessa¹, Simon C. O. Glover⁷, Brent Groves^{8,9}, Annie Hughes^{10,11}, J. M. Diederik Kruijssen¹², Miguel Querejeta¹³, Andreas Schruba¹⁴, Frank Bigiel¹⁵, Guillermo A. Blanc^{16,17}, Mélanie Chevance¹², Dario Colombo¹⁸, Christopher Faesi¹, Jonathan D. Henshaw¹, Cinthya N. Herrera¹⁹, Daizhong Liu¹, Jérôme Pety^{19,20}, Johannes Puschig¹⁵, Toshiki Saito¹, Jiayi Sun⁴, and Antonio Usero¹³

¹ Max-Planck-Institut für Astronomie, Königstuhl 17 D-69117 Heidelberg, Germany

² Sterrenkundig Observatorium, Universiteit Gent, Krijgslaan 281 S9, B-9000 Gent, Belgium

³ Department of Physics, University of Alberta, Edmonton, AB, Canada

⁴ Department of Astronomy, The Ohio State University, 140 West 18th Avenue, Columbus, Ohio 43210, USA

⁵ European Southern Observatory, Karl-Schwarzschild Straße 2, D-85748 Garching bei München, Germany

⁶ Univ Lyon, Univ Lyon1, ENS de Lyon, CNRS, Centre de Recherche Astrophysique de Lyon UMR5574, F-69230 Saint-Genis-Laval, France

⁷ Institut für Theoretische Astrophysik, Zentrum für Astronomie der Universität Heidelberg, Albert-Ueberle-Strasse 2, D-69120 Heidelberg, Germany

⁸ Research School of Astronomy and Astrophysics, Australian National University, Canberra, ACT 2611, Australia

⁹ International Centre for Radio Astronomy Research, The University of Western Australia, Crawley, WA 6009, Australia

¹⁰ Université de Toulouse, UPS-OMP, F-31028 Toulouse, France

¹¹ CNRS, IRAP, Av. du Colonel Roche BP 44346, F-31028 Toulouse cedex 4, France

¹² Astronomisches Rechen-Institut, Zentrum für Astronomie der Universität Heidelberg, Mönchhofstraße 12-14, D-69120 Heidelberg, Germany

¹³ Observatorio Astronómico Nacional (IGN), C/Alfonso XII 3, Madrid E-28014, Spain

¹⁴ Max-Planck-Institut für Extraterrestrische Physik, Giessenbachstraße 1, D-85748 Garching bei München, Germany

¹⁵ Argelander-Institut für Astronomie, Universität Bonn, Auf dem Hügel 71, D-53121 Bonn, Germany

¹⁶ The Observatories of the Carnegie Institution for Science, 813 Santa Barbara Street, Pasadena, CA, 91101, USA

¹⁷ Departamento de Astronomía, Universidad de Chile, Camino del Observatorio 1515, Las Condes, Santiago, Chile

¹⁸ Max-Planck-Institut für Radioastronomie, Auf dem Hügel 9, D-53121 Bonn, Germany

¹⁹ Institut de Radioastronomie Millimétrique, 300 rue de la Piscine, F-38406 Saint-Martin-d'Hères Cedex, France

²⁰ Sorbonne Université, Observatoire de Paris, Université PSL, CNRS, LERMA, F-75014, Paris, France

Received 2019 November 2; revised 2020 May 9; accepted 2020 May 16; published 2020 July 9

Abstract

We present kinematic orientations and high-resolution (150 pc) rotation curves for 67 main-sequence star-forming galaxies surveyed in CO (2–1) emission by PHANGS–ALMA. Our measurements are based on the application of a new fitting method tailored to CO velocity fields. Our approach identifies an optimal global orientation as a way to reduce the impact of nonaxisymmetric (bar and spiral) features and the uneven spatial sampling characteristic of CO emission in the inner regions of nearby galaxies. The method performs especially well when applied to the large number of independent lines of sight contained in the PHANGS CO velocity fields mapped at 1'' resolution. The high-resolution rotation curves fitted to these data are sensitive probes of mass distribution in the inner regions of these galaxies. We use the inner slope as well as the amplitude of our fitted rotation curves to demonstrate that CO is a reliable global dynamical mass tracer. From the consistency between photometric orientations from the literature and kinematic orientations determined with our method, we infer that the shapes of stellar disks in the mass range of $\log(M_*(M_\odot)) = 9.0\text{--}10.9$ probed by our sample are very close to circular and have uniform thickness.

Unified Astronomy Thesaurus concepts: [Galaxy dynamics \(591\)](#); [Interstellar medium \(847\)](#); [Molecular clouds \(1072\)](#)

Supporting material: machine-readable table

1. Introduction

Modern extragalactic CO surveys measure the properties of molecular gas at cloud (50–100 pc) scales with high completeness across large areas (e.g., Schinnerer et al. 2013; Freeman et al. 2017; Leroy et al. 2017; Sun et al. 2018). This makes it possible to place cloud-scale molecular gas properties in the context of the global kinematic response to the galactic potential, offering a view of the factors that influence the organization of the molecular gas and the star formation that occurs within it. One of the strengths of this approach is the ability to use one data set to characterize the density distribution, the local gas motions, and the galaxy dynamical mass for any single galaxy over a range of spatial scales.

There are several factors that make the cold molecular phase of the interstellar medium (ISM) a good tracer of the global

dynamics of a galaxy. For nearby galaxies, information about the molecular gas kinematics can typically be obtained out to the edge of the optical disk (e.g., Schruba et al. 2011 report extents in the range of ~ 0.3 to $1.3 R_{25}$). They reveal a projection of motion that can be used to infer the orientation of the galaxy with respect to the line of sight, as well as the speed at which material orbits around the galaxy center. The projected velocities in this case are an almost direct probe of the galaxy's underlying mass distribution given the dissipative nature of molecular gas, which results in characteristically low velocity dispersions ($1\text{--}20 \text{ km s}^{-1}$) in the disks of typical nearby galaxies (e.g., Combes & Becquaert 1997; Helfer et al. 2003; Colombo et al. 2014; Sun et al. 2018; Boizelle et al. 2019). This feature has prompted the use of high-resolution kinematic maps of the inner portions of CO disks observed with the Atacama Large Millimeter/submillimeter Array

(ALMA) to reconstruct the masses of supermassive black holes in the centers of nearby galaxies (e.g., Davis & McDermid 2017; Onishi et al. 2017; Davis et al. 2018).

The dissipative quality of the gas also leads to a distinctly strong response to underlying nonaxisymmetric components in the gravitational potential (e.g., Roberts & Stewart 1987; Kim & Ostriker 2006; Dobbs & Pringle 2009). Bar and spiral arm features yield recognizable deviations from circular motions in velocity field maps that provide powerful constraints on the structure of the ISM and its organization by the local galactic environment.

Yet, as a global dynamics tracer, molecular gas kinematics are confronted with issues that become more obvious at high spatial resolutions: because the molecular phase traces the material at densities where gas begins to decouple from the background potential, thus forming weakly self-gravitating clouds (e.g., Meidt et al. 2018), molecular gas emission is primarily confined to spiral arms, bars, or collections of individual clouds. The gas in these regions reveals a strong contribution from noncircular streaming motions, more evident at higher spatial resolution (e.g., Meidt et al. 2013; Colombo et al. 2014). Without additional modeling, measurements of disk orientation based on velocity maps thus exhibit recognizable deviations from their true values. In these cases, rotational velocities also reflect the added contribution from noncircular motions, leading to systematic offsets in the inferred rotation curve (e.g., Fathi et al. 2005; van de Ven & Fathi 2010; Chemin et al. 2015, 2016).

In this paper, we present global disk orientations and rotation curves from $\sim 1''$ PHANGS–ALMA²¹ CO data extending on average out to $\sim 0.7 R_{25}$ for 67 local star-forming galaxies. This is the largest such compilation of CO rotation curves to date (c.f., Sofue & Rubin 2001) and complements the rich kinematics constraints offered by a growing number of stellar and multiphase gas kinematics surveys in the local universe (de Blok et al. 2008; Epinat et al. 2008; Chung et al. 2009; Lelli et al. 2016; Kalinova et al. 2017; Korsaga et al. 2018; Levy et al. 2018).

We use an approach that is optimized for kinematic tracers with low spatial filling factor that probe the central regions of galaxies at high spatial resolution. This makes it ideally suited for the wide-field CO data now regularly produced by ALMA and NOEMA. Our technique incorporates many of the same elements implemented in the wealth of existing algorithms that fit 2D and 3D kinematic data (Van Albada et al. 1985; Begeman 1987; Schoenmakers 1999; Simon et al. 2003; Krajnović et al. 2006; Józsa et al. 2007; Spekkens & Sellwood 2007; Bouche et al. 2015; di Teodoro & Fraternali 2015; Kamphuis et al. 2015; Peters et al. 2017; Oh et al. 2018). To overcome the complications of fitting CO velocity fields, we introduce a new element that involves fitting orientations to all lines of sight at once. This maximizes constraints from regions that provide an unbiased probe of circular motion.

This paper is structured as follows: we discuss the observational data used as well as our sample selection in Section 2. This is followed by a description of our fitting technique in Section 3. Our results are presented in Section 4, followed by a discussion of our findings in Section 5. Finally, we present our conclusions in Section 6.

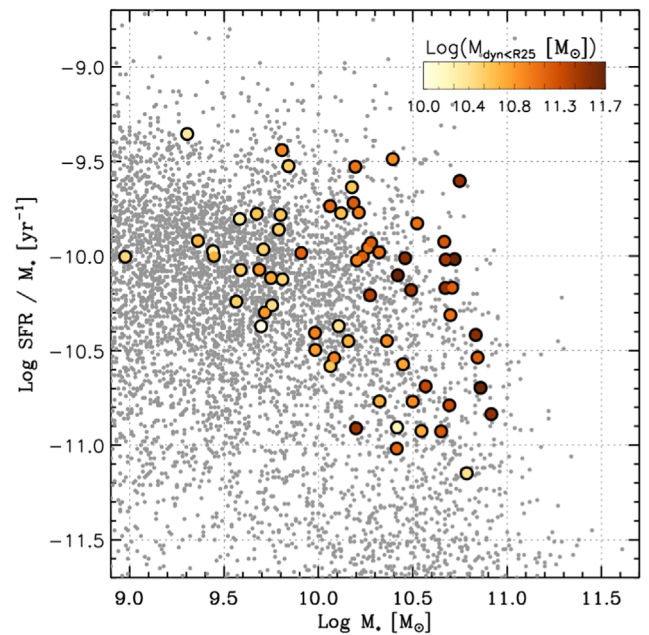


Figure 1. The subset of the PHANGS–ALMA sample used for this paper (colored symbols) in the M_* –sSFR plane. The color-coding indicates the total dynamical mass within R_{25} ($M_{\text{dyn},R_{25}}$; see Section 4.4.3). The underlying population of star-forming galaxies taken from Leroy et al. (2019) is shown as gray symbols (see text for details). Our kinematic sample spans a large range of stellar masses, SFRs, and ratios of stellar-to-total dynamical masses, while sampling well the underlying population of local main-sequence galaxies.

2. Observations and Sample

2.1. ALMA CO (2–1) Observations and Sample Selection

This work exploits observations of the PHANGS–ALMA sample of nearby galaxies with CO (2–1) emission mapped with ALMA at high ($\sim 1''$) angular resolution. Details of the sample selection, ALMA observations, and data processing are described in detail in A. K. Leroy et al. (2020, in preparation). In short, PHANGS–ALMA is designed to target 74 massive ($\log(M_*/M_\odot) > 9.75$), actively star-forming ($\log(\text{sSFR}/\text{Gyr}^{-1}) > -11$), moderately inclined ($i < 75^\circ$) galaxies that are accessible to ALMA (see Figure 1). Furthermore, PHANGS targets are chosen to be nearby (distance < 17 Mpc) such that the survey’s nominal resolution of $1''$ accesses linear scales of about 100 pc. The PHANGS–ALMA sample comprises observations from several ALMA programs: 2013.1.00650.S, P.I. E. Schinnerer; 2013.1.00803.S, P.I. D. Espada; 2013.1.01161.S, P.I. K. Sakamoto; 2015.1.00925, P.I. G. Blanc; 2015.1.00956, P.I. A. K. Leroy; 2017.1.00392.S, P.I. G. Blanc; 2017.1.00886.L, P.I. E. Schinnerer; 2018.1.01651.S, P.I. A. K. Leroy.

Each galaxy is observed by one or more rectangular mosaics. We combine observations of the mosaicked region from all three ALMA arrays to produce fully sampled images, including data from the 12 m array (designated “12 m”), the Morita Atacama Compact Array (designated “7 m”), and the 12 m telescopes configured to observe as single-dish telescopes, providing estimates of the total power (designated “TP”). The 12 m data are obtained from array configurations C43-1 or C43-2. We calibrate the 12 m and 7 m data using the observatory-provided pipeline, and we calibrate and image the TP data using the scripts developed by Herrera et al. (2020). We imaged the 12 m + 7 m data with CASA v5.4 using an emission-mask-based cleaning scheme as described in

²¹ www.phangs.org

A. K. Leroy et al. (2020, in preparation). The interferometer data are merged with the single-dish data using the FEATHER task within CASA, producing a well-sampled map that is then corrected for the primary beam power pattern. We convolve the maps to have circular synthesized beams. The 1σ noise level in the maps is approximately 0.3 K in a 2.5 km s^{-1} channel. There is significant (30%) variation in beam size and survey depth across the different galaxies, arising from the sky positions of the galaxy, the atmospheric conditions at ALMA, and the configurations used in the observation. The imaging process yields a spectral-line data cube where the spectral axis is the radial velocity determined by using the Doppler effect with the radio convention. The velocities are referenced to the kinematic local standard of rest (LSRK) frame.

From the spectral-line data cubes, we generate two-dimensional integrated intensity maps as well as estimates for the mean line-of-sight velocity that we will use for rotation curve fitting. We begin by making an empirical estimate of the noise level at each point in the cube, first measuring the noise as the median absolute deviation of the pixels for each spectrum, iteratively rejecting positive outliers associated with the signal. We then smooth the spatial noise estimate over ~ 3 beam FWHMs. At this point, we calculate the relative variation of the noise level in each spectral channel that, in combination with the noise map, yields an estimate of the noise level at every point in the data cube. Next, we identify the signal at every point in the map, using a two-stage masking process. We first identify all regions with $T_B > 3.5\sigma$ in three consecutive channels. These regions are then dilated in three-dimensional space to all connected regions that show $T_B > 2\sigma$ in two consecutive channels. We refer to this masking process as the “strict” mask. This masking process is then repeated on a data cube that is convolved to 500 pc linear resolution. This latter process identifies low-surface-brightness emission. We build a “broad” mask by identifying pixels in the cube that are associated with signal in either the low- or high-resolution mask.

Using these masks, we calculate the integrated intensity maps (I_{CO} or “moment-0” maps) for each position as

$$I_{\text{CO}}(x, y) = \sum_k T_B(x, y, v_k) \mathcal{M}(x, y, v_k) \delta v, \quad (1)$$

where \mathcal{M} is the mask (value of 1 for signal, 0 otherwise) and δv is the channel width. We use a moment-based estimator for the line-of-sight velocity:

$$V_{\text{obs}}(x, y) = \frac{1}{I_{\text{CO}}} \sum_k v_k T_B(x, y, v_k) \mathcal{M}(x, y, v_k) \delta v. \quad (2)$$

We create strict and broad maps for the integrated intensity and observed velocity. The strict maps show lower flux recovery but high-quality V_{obs} maps. The broad maps have better flux recovery but occasionally show spurious features in their velocity maps associated with noise. We build final V_{obs} maps by using the broad maps but we remove positions where (1) the $I_{\text{CO, broad}}$ is less than $2\times$ its associated uncertainty or (2) the velocity field at high resolution differs from the velocity field measured at 500 pc resolution by more than 30 km s^{-1} .

Out of the sample of 74 PHANGS–ALMA targets, we select 72 galaxies for which high-resolution moment maps (i.e., either combined $12 \text{ m} + 7 \text{ m} + \text{TP}$ or $12 \text{ m} + 7 \text{ m}$) are available. We reject one source with a high-resolution moment map that

contains no detected pixel above the applied signal-to-noise ratio (S/N) cut (IC 5332), and one source (NGC 3239) that is only detected within the very central region (at radii $\leq 2''$). Three sources (NGC 4424, NGC 4694, and NGC 4731) show V_{obs} maps that suggest no ordered rotational motion within the detected area and are subsequently rejected. We thus have 67 PHANGS galaxies with high-resolution CO maps for analysis. The position of our sample in the M_* versus specific star formation rate (sSFR = SFR/M_*) plane is shown in Figure 1, and the basic properties are presented in Table 1. Note that, due to updates on distances and stellar mass-to-light ratio (M/L), our sample expands to lower stellar masses than implied by the initial stellar mass cut of PHANGS–ALMA quoted above.

We adopt global galaxy parameters for the galaxies as outlined in A. K. Leroy et al. (2020, in preparation). We use the stellar mass of a galaxy (M_*), the global star formation rate (SFR), and distance measurements from the $z = 0$ Multi-wavelength Galaxy Survey (z0MGS) compilation of data (Leroy et al. 2019). HyperLEDA²² (Paturel et al. 2003; Makarov et al. 2014) values are used for the radius of the 25 mag arcsec⁻² isophote (R_{25}). Measurements of effective half-light radii (R_e) are calculated from the cumulative flux distribution determined on the NIR WISE1 maps (Leroy et al. 2019).

2.2. Sample Demographics

This section summarizes the properties of the observed ALMA velocity fields used for this study which are important to the design of our fitting method. We have examined the impact of these properties on the results of our method by performing extensive tests on mock galaxy velocity fields. These tests have suggested a number of quality assessment criteria that we present and discuss in detail later in Section 4.2.

2.2.1. Radial Extent of the CO Emission

CO emission is an ideal tracer of the kinematics of the inner disks of galaxies but may provide a limited probe of outer disk dynamics, depending on the (finite) extent of the CO emission. In practice, the outer probed edge of our CO velocity fields is determined by the drop in CO signal with galactocentric radius and the finite extent of the PHANGS maps. We quantify the impact of finite spatial extent by measuring the ratio between the maximum galactocentric radius out to which we detect the CO(2–1) line emission, $R_{\text{CO,max}}$, and the outer radius of the optical disk, R_{25} . To derive $R_{\text{CO,max}}$, we bin the observed velocity field in elliptical annuli that have a width of three pixels (corresponding to about the observed FWHM). The annuli are centered on the photometric center (see Table 1) and oriented according to our best-fit kinematic orientations (see Section 4.3). We define $R_{\text{CO,max}}$ as the radius at which the total number of detected pixels within a given annulus falls below 10. Varying this threshold by a factor of 2 changes $R_{\text{CO,max}}$ by only 4% on average.

The distribution of $R_{\text{CO,max}}/R_{25}$ for our sample, shown in the left panel of Figure 2, has a range of 0.26–1.2, and median of 0.72. Our data thus probe out to ~ 3.6 CO scale lengths (following Schrubba et al. 2011), thereby characterizing $\sim 90\%$ of the total CO emission (Schruba et al. 2011; Puschnig et al. 2020). Moreover, our maps typically probe beyond radii where the rotation curve flattens out (which happens on average

²² <http://leda.univ-lyon1.fr/>

Table 1
Basic Properties of the Kinematic PHANGS Sample

ID	R.A. ¹ (deg)	Decl. ¹ (deg)	Distance (Mpc)	V_{sys}^2 (km s ⁻¹)	ϕ_{phot}^3 (deg)	i_{phot}^4 (deg)	f_{CO}^5 (arcsec)	$\frac{R_{\text{bar}}}{R_{\text{CO,max}}}$	$\frac{R_{\text{CO,max}}}{R_{25}}$
IC 1954	52.87971	-51.90486	15.2	1062.9	61.0	57.7	0.46	0.09	0.84
IC 5273	344.86118	-37.70284	14.7	1293.9	229.0	44.3	0.27	0.22	0.97
NGC 0628	24.17385	15.78364	9.8	658.5	0.1	28.9	0.29	0.00	0.55
NGC 0685	26.92845	-52.76198	16.0	1359.7	99.2	38.6	0.21	0.25	0.87
NGC 1087	41.60492	-0.49872	14.4	1522.7	1.4	51.4	0.36	0.20	0.94
NGC 1097	41.57896	-30.27467	14.2	1269.4	126.5	48.6	0.25	0.52	0.57
NGC 1300	49.92081	-19.41111	26.1	1578.2	286.1	31.8	0.10	0.68	0.67
NGC 1317	50.68454	-37.10379	19.0	1948.5	200.3	35.0	0.48	0.19	0.35
NGC 1365	53.40152	-36.14040	18.1	1638.3	210.7	55.4	0.14	0.52	0.49
NGC 1385	54.36901	-24.50116	22.7	1497.3	172.3	49.7	0.34	0.00	0.72
NGC 1433	55.50619	-47.22194	16.8	1075.3	204.3	28.6	0.09	0.05	0.75
NGC 1511	59.90246	-67.63392	15.6	1334.9	304.0	71.1	0.31	0.20	0.95
NGC 1512	60.97557	-43.34872	16.8	897.7	254.5	42.5	0.12	0.62	0.45
NGC 1546	63.65122	-56.06090	18.0	1252.9	147.4	67.4	0.46	0.00	0.72
NGC 1559	64.40238	-62.78341	19.8	1295.3	245.1	54.0	0.31	0.09	1.00
NGC 1566	65.00159	-54.93801	18.0	1501.8	200.9	30.4	0.26	0.27	0.61
NGC 1672	71.42704	-59.24726	11.9	1338.8	148.5	23.7	0.19	0.48	0.83
NGC 1792	76.30969	-37.98056	12.8	1210.6	316.1	60.7	0.34	0.00	0.81
NGC 1809	75.52066	-69.56794	15.0	1300.6	144.8	80.5	0.10	0.00	0.57
NGC 2090	86.75787	-34.25060	11.8	922.1	196.5	71.7	0.44	0.00	0.53
NGC 2283	101.46997	-18.21080	10.4	840.8	0.1	44.2	0.18	0.14	1.05
NGC 2566	124.69003	-25.49952	23.7	1637.9	235.6	48.5	0.15	0.46	1.02
NGC 2775	137.58396	7.03807	17.0	1354.1	163.5	34.2	0.30	0.00	0.58
NGC 2835	139.47044	-22.35468	10.1	886.5	0.3	56.4	0.07	0.23	0.48
NGC 2903	143.04212	21.50084	8.5	555.3	199.6	63.5	0.28	0.25	0.75
NGC 2997	146.41164	-31.19109	11.3	1086.9	96.6	54.3	0.42	0.06	0.62
NGC 3059	147.53400	-73.92219	19.8	1258.0	-5.0	21.2	0.30	0.22	0.77
NGC 3137	152.28116	-29.06430	14.9	1106.3	3.9	47.2	0.30	0.00	0.53
NGC 3351	160.99064	11.70367	10.0	778.0	188.4	45.1	0.25	0.41	0.58
NGC 3507	165.85573	18.13552	20.9	975.6	80.1	27.5	0.27	0.34	0.85
NGC 3511	165.84921	-23.08671	9.9	1105.4	258.4	72.1	0.30	0.11	0.94
NGC 3521	166.45240	-0.03595	11.2	800.9	342.3	66.2	0.44	0.00	0.89
NGC 3596	168.77581	14.78707	10.1	1192.4	108.2	16.9	0.27	0.00	0.66
NGC 3621	169.56792	-32.81260	6.6	730.1	341.2	67.5	0.34	0.00	0.83
NGC 3626	170.01588	18.35684	20.0	1479.5	163.2	46.6	0.40	0.88	0.26
NGC 3627	170.06252	12.99150	10.6	720.9	166.2	55.7	0.40	0.37	0.58
NGC 4207	183.87681	9.58493	16.8	608.6	121.3	70.5	0.27	0.00	0.89
NGC 4254	184.70680	14.41641	16.8	2407.9	76.6	36.2	0.33	0.00	1.13
NGC 4293	185.30346	18.38257	16.0	901.6	64.0	65.0	0.16	1.32	0.32
NGC 4298	185.38651	14.60611	16.8	1128.4	311.1	56.4	0.55	0.00	1.21
NGC 4303	185.47888	4.47374	17.6	1566.9	323.6	24.2	0.56	0.36	0.49
NGC 4321	185.72886	15.82230	15.2	1573.9	158.2	33.2	0.30	0.04	1.03
NGC 4457	187.24593	3.57062	15.6	884.9	66.4	17.4	0.48	0.78	0.50
NGC 4496a	187.91358	3.93962	14.9	1730.4	62.4	29.1	0.12	0.29	0.80
NGC 4535	188.58459	8.19797	15.8	1962.1	202.8	22.4	0.33	0.28	0.54
NGC 4536	188.61278	2.18824	15.2	1807.3	305.5	67.7	0.25	0.19	0.84
NGC 4540	188.71193	15.55172	16.8	1284.1	56.0	11.8	0.34	0.41	0.68
NGC 4548	188.86024	14.49633	16.2	481.5	149.2	38.3	0.25	0.52	0.69
NGC 4569	189.20759	13.16287	16.8	-219.5	24.8	69.7	0.33	0.61	0.58
NGC 4571	189.23492	14.21733	14.9	335.7	264.1	14.1	0.28	0.00	0.74
NGC 4579	189.43138	11.81822	16.8	1516.8	92.1	41.3	0.49	0.37	0.72
NGC 4654	190.98575	13.12672	16.8	1043.4	120.7	58.6	0.37	0.22	0.91
NGC 4689	191.93990	13.76272	16.8	1608.4	163.7	35.3	0.41	0.00	0.70
NGC 4781	193.59916	-10.53712	15.3	1262.3	290.8	61.5	0.33	0.18	0.92
NGC 4826	194.18184	21.68308	4.4	407.6	295.9	58.2	0.22	0.00	0.38
NGC 4941	196.05461	-5.55154	14.0	1111.2	203.5	39.4	0.46	0.00	0.83
NGC 4951	196.28213	-6.49382	12.0	1177.6	91.5	76.1	0.24	0.00	0.83
NGC 5042	198.87920	-23.98388	12.6	1389.1	195.9	57.4	0.28	0.30	0.53
NGC 5068	199.72808	-21.03874	5.2	671.2	300.1	27.0	0.05	0.17	0.94
NGC 5134	201.32726	-21.13419	18.5	1755.7	300.0	4.9	0.24	0.79	0.70
NGC 5248	204.38336	8.88519	12.7	1152.3	103.9	37.8	0.25	0.00	0.98
NGC 5530	214.61380	-43.38826	11.8	1193.1	306.5	66.5	0.30	0.00	0.70
NGC 5643	218.16991	-44.17461	11.8	1190.0	320.6	29.9	0.41	0.45	0.76

Table 1
(Continued)

ID	R.A. ¹ (deg)	Decl. ¹ (deg)	Distance (Mpc)	V_{sys} ² (km s ⁻¹)	ϕ_{phot} ³ (deg)	i_{phot} ⁴ (deg)	f_{CO} ⁵ (arcsec)	$\frac{R_{\text{bar}}}{R_{\text{CO,max}}}$	$\frac{R_{\text{CO,max}}}{R_{25}}$
NGC 6300	259.24780	-62.82055	13.1	1108.7	118.6	53.2	0.32	0.16	0.79
NGC 6744	287.44208	-63.85754	9.5	851.4	15.4	53.5	0.14	0.36	0.53
NGC 7456	345.54306	-39.56941	7.9	1200.7	22.9	75.2	0.20	0.00	0.69
NGC 7496	347.44703	-43.42785	18.7	1650.3	213.2	9.0	0.37	0.44	0.80

Note. 1: Adopted photometric galaxy center; 2: prior of systemic velocity; 3: prior of photometric disk position angle; 4: prior of photometric disk inclination; 5: spatial CO covering fraction.

within $0.1 R_{25}$, as discussed in Section 4.4.1). For a subset of galaxies, however, the CO emission traces only the part of the galaxy where rotational velocities rise steeply. The outer asymptotic rotation curve behavior is thus unconstrained in these cases and fits to the inner solid-body motion alone yield poorly constrained disk orientations and inner rotation curves.

2.2.2. Impact of the Clumpiness of the CO Spatial Distribution on Velocity Field Recovery

The low area filling factor of CO emission can have consequences for the observational recovery of velocity information in PHANGS-ALMA moment maps. Depending on the surface brightness sensitivity limit, using a molecular emission-line tracer can favor sight lines that sample narrow, high-density contrast features organized by bars and spiral arms. This leads to nonaxisymmetric or incomplete azimuthal coverage especially when, e.g., lines of sight in the lower density inter-arm regions (where motion is expected to be more nearly circular) are underrepresented. Clumpiness can further heighten the sparseness of the velocity coverage.

The middle panel of Figure 2 illustrates the velocity field coverage (see Section 2.1) throughout the sample, defined as the fraction of detected pixels inside $R_{\text{CO,max}}$. The median CO covering fraction in the sample is about 30%. This is strongly influenced by typically poorer coverage toward the outermost radii probed in each map. This is also portrayed in Figure 3, which tracks the drop in CO brightness with galactocentric radius. The median covering fraction drops smoothly with R/R_{25} and typically becomes zero at around $0.6\text{--}0.8R_{25}$. Figure 3 also highlights a strong variation of the CO covering fraction among our sample at a given radius.

2.3. The Structure and Orientation of the Underlying Stellar Disk

For PHANGS targets, extensive imaging data available for the sample provides a complementary view of the inner gravitational potential. These data provide key information about the disk structure and orientation that we use to inform our fitting and the interpretation of our results.

2.3.1. Photometric Priors on Disk Orientation and Centering for the Sample

As will be described in more detail in the next section, our method relies on prior information about the disk orientation (i.e., position angle²³ ϕ and inclination i), center position of the

disk, and systemic velocity V_{sys} . In our fitting process explained below, we redetermine ϕ , i , and V_{sys} for each galaxy while keeping the center position fixed.

Where possible, we adopt photometric priors from the Spitzer/S⁴G survey (Sheth et al. 2010; Muñoz-Mateos et al. 2013; Querejeta et al. 2015), covering 54 sources from our total sample. We made this catalog our primary choice due to the combination of good angular resolution and excellent imaging depth. We adopt central coordinates, position angles, and inclinations from the Salo et al. (2015) catalog based on isophotal analysis on Spitzer 3.6 μm images. Values for ϕ and i measured through photometry are hereby referred to as ϕ_{phot} and i_{phot} , respectively. These are determined from profiles of ellipticity and position angle of the outer galaxy isophotes, where the influence of bars and/or spiral structures is minimized. To convert the axial ratio q implied by the quoted ellipticity η (with $q = 1 - \eta$) into i_{phot} , we use the relation

$$\cos(i_{\text{phot}}) = \sqrt{\frac{q^2 - q_{\text{min}}^2}{1 - q_{\text{min}}^2}}. \quad (3)$$

Here, q_{min} is the intrinsic edge-on thickness of the disk, which we fix to a value of 0.25 (see van der Wel et al. 2014). Adopting a thin disk with $q_{\text{min}} = 0.1$ leads to smaller values of i_{phot} by at most 2^o5 for the range of inclinations covered by our sample. By comparing the 3.6 μm S⁴G orientations with the HyperLEDA orientations (defined in optical bands) for this subset of the sample, we obtain a rough (10^o) estimate of typical uncertainties on ϕ_{phot} and i_{phot} .

For galaxies not covered by S⁴G (13 sources), we adopt the central positions from the 2MASS/LGA catalog (Jarrett et al. 2003) based on J -/ H -/ K -band imaging if available, and from HyperLEDA otherwise. Galaxy orientations for non-S⁴G sources are adopted from HyperLEDA. For sources with no ϕ_{phot} measurement available within HyperLEDA, we use the respective value from 2MASS/LGA.

As a consistency check on the positional accuracy of our photometric centers, we computed the offsets between the central positions of both S⁴G and 2MASS catalogs for our covered sources. We find good agreement between these central positions, with a 1σ scatter of about 1". We also confirm by visual inspection that there is consistency between the adopted photometric center and the kinematic center of our CO velocity fields. Prior systemic velocities for our sources are taken from the collection of HI measurements from the HyperLEDA database.

Table 1 lists the basic properties of our sample including the photometric priors.

²³ The position angle follows the standard convention of being measured east of north on the celestial sphere.

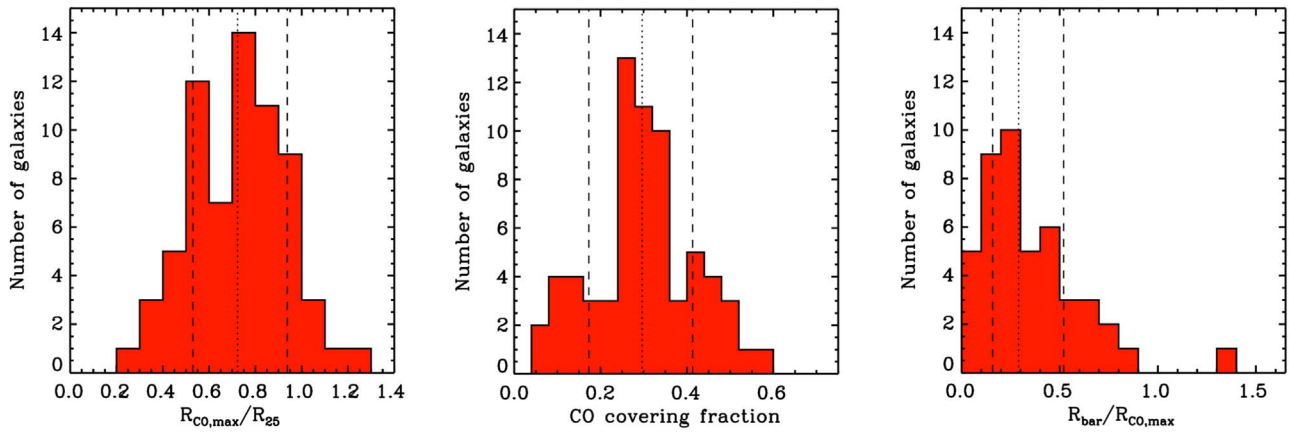


Figure 2. Left: distribution of the ratio between the extent of the ALMA CO velocity fields ($R_{\text{CO,max}}$) and the disk size (R_{25}). Middle: distribution of spatial coverage filling factor in the CO velocity fields at $\sim 1''$ resolution. Right: distribution of the ratio between bar length R_{bar} and $R_{\text{CO,max}}$. Shown is only the subset of barred galaxies (45 out of 67 systems). In all panels, the median of the distribution is shown as a dotted line, and the 16th and 84th percentiles are shown as dashed lines, respectively.

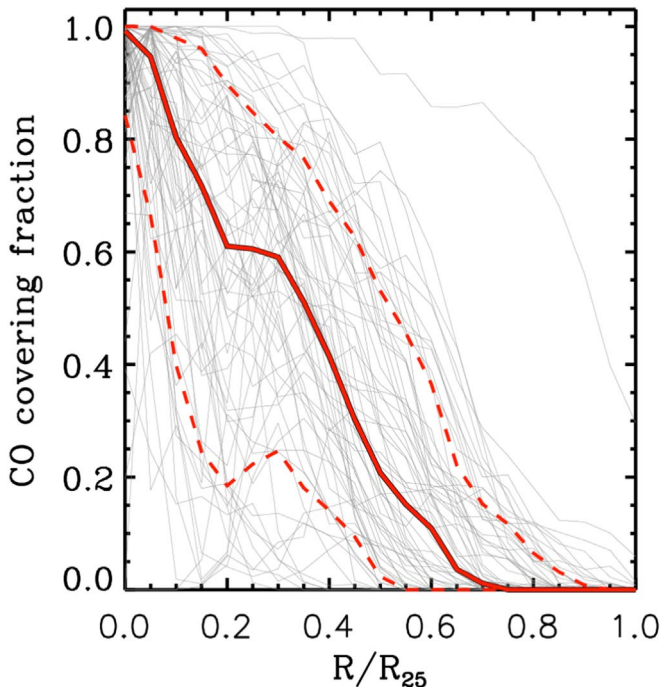


Figure 3. Spatial CO covering fraction per radial bin vs. R/R_{25} for our sample. The median and scatter based on the 16th and 84th percentiles are shown as solid and dashed red lines, respectively. Individual galaxies are shown as gray lines.

2.3.2. Central Bar and Bulge Properties

One of the main goals of this work is to correlate the inner stellar structures hosted by star-forming galaxies with the kinematics of their molecular gas disks. Thus, we collect estimates of stellar bar length (R_{bar}), and bulge-to-total (B/T) ratio mainly based on Spitzer/IRAC $3.6\ \mu\text{m}$ images. R_{bar} measurements for the PHANGS–ALMA sample are compiled by M. Querejeta et al. (2020, in preparation), who combine previous catalogs from Herrera-Endoqui et al. (2015) with additional $3.6\ \mu\text{m}$ imaging for a subset of PHANGS–ALMA targets not covered by S⁴G, as well as existing literature measurements. B/T ratios are available from the two-component decompositions performed on S⁴G images by Salo et al. (2015).

2.3.3. The Prominence of Stellar Bars

Next, we inspect the frequency and properties of stellar bars in our sample, as the strongest and most prominent of these can have a major impact on the appearance of inner stellar and gaseous velocity fields due to their tumbling nonaxisymmetric potential (e.g., Wong et al. 2004; Fathi et al. 2005; Boone et al. 2007; Hunt et al. 2008; Sormani et al. 2015).

The majority (67%) of our sample are barred systems, with the more massive galaxies hosting a higher fraction of bars. In the right panel of Figure 2, we show the distribution of $R_{\text{bar}}/R_{\text{CO,max}}$ for the strongly barred subset of our sample (i.e., bar ellipticity $\epsilon > 0.4$; Jogee et al. 2004). Most of the CO fields extend beyond the bar, offering good constraints of the CO kinematics from within the disk-dominated portion of the map. However, we note that galaxies for which the bar is strong and covers a large portion of the observed CO map pose strong limitations to our method for constraining the disk orientation and are therefore treated with care in our subsequent analysis.

3. Methods

In this section, we present an overview of the method used to determine the kinematic properties of the PHANGS galaxies. We first outline the considerations that led to the development of the method and then we present the details of the implementation.

3.1. Considerations for Modeling CO Velocity Fields

Our implementation is tailored to three features of our data. First, our observations are confined to the central part of the galactic disk, where a flat circular disk is a good approximation to the galactic geometry. Second, the CO emission is clumpy, requiring a method that is robust to missing data. Finally, the molecular gas emission highlights spiral arms and bars where noncircular motions can be significant. We address these considerations by using a Bayesian framework, sampling a probability density function describing the data using a Markov Chain Monte Carlo (MCMC) sampler.

Most existing techniques to determine the kinematic properties of galaxies build on the basic tilted-ring model of the line-of-sight velocity field first introduced by Rogstad et al. (1974; see also Bosma 1978; Begeman 1987). This yields measurements of ϕ , i , and rotational velocity in a series of radial bins. This approach

works well for smooth, extended HI emission (de Blok et al. 2008; Trachternach et al. 2008; Schmidt et al. 2016) and can also be formulated using a Bayesian approach (Oh et al. 2018). For applications to kinematic tracers characterized by sparseness or noncircular motions, the tilted-ring approach has tended to require careful supervision (e.g., Fathi et al. 2005; Józsa et al. 2007; Spekkens & Sellwood 2007; van de Ven & Fathi 2010; Colombo et al. 2014). As a kinematic tracer, CO emission differs from atomic gas. Even though the CO emission is sparser than the atomic gas, it has the advantage of tracing a thinner disk and arises from a more centrally concentrated area, so that it avoids the warps and radial flows that are seen in outer atomic gas disks (see, e.g., Schmidt et al. 2016). We can thus approximate the CO emission as arising from a thin, circular disk, which simplifies our approach to determining disk orientation parameters (ϕ and i).

On the other hand, CO emission is frequently organized into features associated with complex noncircular motions, such as spiral arms and bars characteristic of the inner disks of nearby galaxies. The sharpness of these features in CO requires more careful treatment than the smoother, puffier atomic gas would across the same region (e.g., Colombo et al. 2014). For kinematic tracers like CO that emphasize noncircular motions, fitting orientation parameters in independent radial bins following the tilted-ring model can be biased by the sparse coverage of the mapped area and an overrepresentation of lines of sight dominated by noncircular motion.

To control for these issues, in this paper we prefer to find globally optimal orientation parameters rather than fitting within individual radial bins. This should be appropriate for the inner-disk environment traced by molecular gas, where genuine warps and twists characteristic of outer disks are uncommon. Thus, in the fitting, the orientation parameters ϕ and i are held constant with radius in our method. The rotational velocities for a given orientation, however, are fitted in a series of radial bins.

This approach works because globally, most lines of sight will probe regions dominated by circular motion, even though noncircular motions may bias any given radial bin. Furthermore, the influence of biased bins tends to be less prominent when averaged across the entire disk, given the change in the magnitude and projected orientation of noncircular motions across typical bar and spiral components.

3.2. Fitting Model CO Velocity Fields with MCMC

Our fitting method assumes that the CO emission arises from a thin, circular disk where the geometry of that disk is described in polar coordinates by a radius (R) and angle measured from the kinematic major axis (θ). At a given radius, we assume that the rotation speed as a function of angle θ is well described by a Fourier series (following Franx et al. 1994).

Thus, the line-of-sight velocity observed in the plane of the sky is then

$$V_{\text{los}} = V_{\text{sys}} + \sum_{j=1}^N [c_j \cos(j\theta) + s_j \sin(j\theta)] \sin i, \quad (4)$$

where the coefficients c_j and s_j vary as a function of galactocentric radius, V_{sys} is the systemic velocity, and the harmonic expansion is truncated at some integer N . This type of expansion has been incorporated into a number of algorithms to date (i.e., Reswri, Schoenmakers 1999; Ringfit, Simon et al. 2003; Kinemetry, Krajnović et al. 2006; DiskFit, Spekkens & Sellwood 2007 and Sellwood & Sánchez 2010) in order to

account for the complex array of (noncircular) motions present in the stellar and gaseous disks of galaxies.

The results in this paper are derived under the assumption of purely circular rotation, with $s_1 = 0$ and with $s_j = 0$ and $c_j = 0$ for $j > 1$. In this case, the model reduces to

$$V_{\text{los}} = V_{\text{sys}} + V_{\text{rot}}(R) \cos \theta \sin i. \quad (5)$$

As we will show in the next section, this basic model performs well using all lines of sight at once to constrain the disk orientation, as in our approach. For the sake of generality, below we refer to the generic order- N harmonic expansion incorporated into our algorithm.

We assume that the relationship between the coordinates in the disk and those observed on the sky are described by single values of i and ϕ . For a given center position of the disk measured in sky coordinates ($X_{\text{cen}}, Y_{\text{cen}}$), we can relate the sky position to the disk position using

$$\cos \theta = \frac{-(X - X_{\text{cen}}) \sin \phi + (Y - Y_{\text{cen}}) \cos \phi}{R} \quad (6)$$

and

$$\sin \theta = \frac{-(X - X_{\text{cen}}) \cos \phi - (Y - Y_{\text{cen}}) \sin \phi}{R \cos i}. \quad (7)$$

Given this model, we view the problem from a Bayesian perspective, seeking the parameters that produce the model rotation surface, V_{los} , that provides the most credible representations of the observed data, V_{obs} . Given our model, V_{los} is determined by the parameter set $\{i, \phi, V_{\text{sys}}, X_{\text{cen}}, Y_{\text{cen}}, c_j, s_j\}$. We could proceed by sampling a likelihood function given the observed data using this full set of parameters to determine the posterior distribution of these parameters. However, this leads to a large number of parameters because c_j and s_j vary as a function of galactocentric radius, increasing the parameter space by $2N \times k$ parameters, where k is the number of parameters required to represent the variation of these harmonic coefficients with radius. We reduce the dimensionality of the problem by optimizing c_j and s_j given $\{i, \phi, X_{\text{cen}}, Y_{\text{cen}}\}$ through a least-squares regression of these harmonic coefficients with radius (Section 3.2.2).

In summary, our procedure adopts the following two elements:

1. Bayesian optimization to calculate the posterior distributions for parameters $i, \phi, X_{\text{cen}}, Y_{\text{cen}}, V_{\text{sys}}$, and σ_0 , and
2. Linear least-squares fit for all additional parameters (including all the harmonic amplitudes) at a given set of $(i, \phi, X_{\text{cen}}, Y_{\text{cen}}, V_{\text{sys}})$, embedded within the above optimization.

This scheme is efficient as it isolates the linear part of the fitting process, reducing the dimensionality of the solution space probed by the MCMC process.

3.2.1. The Posterior Distribution

We adopt a log-likelihood for the posterior distribution of the parameters given our data:

$$l(i, \phi, V_{\text{sys}}, X_{\text{cen}}, Y_{\text{cen}}, \sigma_0^2) \propto - \sum_{X,Y} \left[\frac{(V_{\text{obs}} - V_{\text{los}})^2}{2w(\sigma_{\text{obs}}^2 + \sigma_0^2)} - \frac{1}{2} \ln(w(\sigma_{\text{obs}}^2 + \sigma_0^2)) \right] + P(i, \phi, V_{\text{sys}}, X_{\text{cen}}, Y_{\text{cen}}, \sigma_0^2). \quad (8)$$

Here, P represents the prior distributions we assume for the parameters. The quantity σ_{obs} (discussed more below) accounts for the observational uncertainties and the factor $1/w$ represents the weight given to each pixel. We have also introduced an excess variance term σ_0^2 that accounts for motions in excess of the measurement uncertainties which are not produced by a rotational model. To estimate the posterior distributions, we sample this log-likelihood using MCMC methods (Section 3.2.3).

The error σ_{obs} in Equation (8) above represents the measurement uncertainty on each V_{los} in the PHANGS CO first-moment map. We compute the median of all pixels in the uncertainty map to define a global σ_{obs} for each galaxy. By assigning a uniform error, we effectively let all pixels in the observed velocity contribute equally (modulo the weight $1/w$) to the fitting process without altering the median S/N of our data.

A more explicit weighting scheme is introduced with the factor $1/w$. We have adopted $1/w = \cos(\theta_{PA})$ weights for all results presented in this paper, where θ_{PA} is the angle measured with respect to the kinematic major axis. This weighting is used to downweight pixels near the minor axis that only weakly constrain circular motion. A number of variations on this weighting scheme that are used in the literature, including a zero-weight wedge around the minor axis and radial weighting, are also incorporated (but not used). We have found that our results are not particularly sensitive to the choice of weighting scheme; orientations measured with uniform weighting do not change significantly ($\lesssim 3\sigma$) compared to our nominal results.

3.2.2. Harmonic Decomposition

To avoid the computational expense of using MCMC to determine the rotation curve, we perform a least-squares fit to determine the harmonic coefficients c_j, s_j in Equation (4). For a given ϕ and $i, V_{\text{sys}}, X_{\text{cen}}, Y_{\text{cen}}$ (and σ_0), we determine these harmonic amplitudes by performing a least-squares regression to the $k = 1 \dots n$ observed values of the velocity within a series of radial bins:

$$\underset{c_j, s_j}{\operatorname{argmin}} \sum_{k=1}^n \frac{1}{\sigma_{\text{obs},k}^2} \times \left(V_{\text{obs},k} - V_{\text{sys}} - \sum_{j=1}^N [c_j \cos(j\theta_k) + s_j \sin(j\theta_k)] \sin i \right)^2. \quad (9)$$

Here, the coefficients c_j, s_j represent the amplitudes of the j th mode, n is the number of pixels in a given bin, and the polar angle of each datum within the disk (θ_k) is set by the orientation parameters. Because the optimization is linear in the coefficients, this calculation is efficient and reduces the dimensionality of the parameter space that the MCMC sample needs to explore.

The algorithm performs this radial decomposition in concentric, annular bins generated from the orientation parameters ϕ and i . The radial bin width along the kinematic major axis is chosen to correspond to the observed FWHM of the circularized ALMA beam. Even at the highest spatial resolutions of our data set, maps contain sufficient numbers of lines of sight per radial bin to yield statistically well-constrained least-squares solutions.

The velocity field model extends out to the edge of the observed velocity field so that, in practice, the least-squares fit

(Equation (9)) occurs across all detected pixels in the PHANGS first-moment map. For each new set of orientation parameters sampled in the full parameter space probed with MCMC, a unique set of radial bins is defined.

Depending on the azimuthal coverage of the outermost bins (i.e., depending on the organization of the emission near the edge of the map), adopting this approach can make the outer bins overly sensitive to minor axis information, which only weakly constrains circular motion. We find that this affects the fitted orientations in only two cases (NGC 4303 and NGC 4826). We therefore truncate the respective velocity fields at outer radii (60'' for NGC 4303 and 75'' for NGC 4826) before we perform our fitting for these galaxies. The impact of incomplete coverage in the outer radial bins is significant on the outer rotation curve, which we address in a later step of the analysis.

3.2.3. MCMC Implementation

Our regression process is performed using MCMC as implemented specifically in the PYTHON EMCEE package (Foreman-Mackey et al. 2013). In this work, we restrict our harmonic decomposition to the lowest-order cosine coefficient, c_1 . We have found that this basic model fit is well-suited to constrain the global ϕ and i given the demographics of the CO emission in the PHANGS–ALMA sample (see Section 2.2) in particular when all lines of sight are included in the fit.

We sample a four-dimensional parameter space defined by ϕ, i, V_{sys} , and excess variance σ_0^2 , leaving the center position ($X_{\text{cen}}, Y_{\text{cen}}$) fixed for this analysis. The σ_0^2 parameter captures systematic differences between the observed velocity field and the assumed model and effectively accommodates for deviations in the adopted measurement uncertainties on each mapped V_{los} . We assume an inverse-Gamma distribution for the excess variance with a characteristic scale $2.5 \text{ km}^2 \text{ s}^{-2}$ so that $\sigma_0^2 \sim \text{InvGamma}(N, 2.5)$, where N is the number of data.

Our approach allows for intrinsic differences between the kinematic and photometric orientations by assuming flat, uninformative priors for ϕ, i , and V_{sys} . Furthermore, we initialize the walkers for ϕ and i in the EMCEE sampler in a uniform distribution with a conservative width of 50° centered at the photometric values ϕ_{phot} and i_{phot} presented in Table 1. The walkers sampling V_{sys} are initialized around the value adopted from HyperLEDA also listed there. This initialization ensures that the parameter space spanned by ϕ and i is sampled to find a global maximum for the log-probability function. Based on extensive testing, we have found that our fits converge stably to the highest probability density regions within the parameter space after an initial 350 ‘‘burn-in’’ steps. Burn-in steps are not used to generate the posterior parameter distribution functions. In total, the EMCEE sampler is run for 1000 steps with 50 walkers.

3.3. Outputs

3.3.1. Orientation Parameters and Their Uncertainties

After the MCMC run has converged, we compute the marginalized posterior distribution functions (PDFs) for our four free parameters from the MCMC chains after the burn-in phase. To determine the best-fit parameters and its respective uncertainties, we compute the median as well as the 16th and 84th percentiles of the cumulative PDF. The median values are taken as the best-fit ϕ and i , and are hereafter referred to as ϕ_{kin}

and i_{kin} to distinguish those from the photometry-based ϕ_{phot} and i_{phot} . The uncertainties implied by the width of the posterior distributions are typically quite small, $\lesssim 0.2^\circ$, representing the formal statistical error in the limit of our applied model.

The statistical uncertainty does not capture the systematic uncertainties that arise through the combination of the PHANGS–ALMA survey coverage and the presence of dynamical structures in the disk (i.e., bar and/or spiral structure). When the motions in the gas associated with these features are left unfitted, they mimic spatial variations in disk orientation that manifest as well-known variations in tilted-ring determinations of ϕ and i with radius in a galaxy, as we also show below. Therefore, we characterize the uncertainties in our analysis using a jackknifing technique, which subsamples the data that is incorporated into the analysis for a given galaxy.

We first divide each observed velocity field into four radial bins using ellipses that are oriented based on the photometric values. Each radial bin corresponds to an annulus of the same width (i.e., $R_{\text{CO,max}}/4$). We then create three jackknife realizations of each velocity field by eliminating two of the four radial bins for a given realization. Next, we rerun our kinematic fits on all three jackknife realizations for a given galaxy. We then compute the mean absolute difference of the best-fit parameters from the jackknives and our best-fit fiducial ϕ_{kin} and i_{kin} . Finally, we convert the values of the mean absolute difference to a representative Gaussian 1σ error by multiplying with a factor of 1.25.

The jackknife uncertainties overall yield median uncertainties of 1.3° and 5.6° on ϕ_{kin} and i_{kin} , respectively. This corresponds to an increase in uncertainty by factors of about 18 and 20 for ϕ and i , respectively, with respect to our formal fitting errors. Thus, our jackknife uncertainties provide a good representation of the significant systematic variations in ϕ_{kin} and i_{kin} not captured by our formal MCMC errors.

In addition, we determine the uncertainties of our best-fit V_{sys} using the jackknife realizations as done for ϕ_{kin} and i_{kin} above. We find an average error in V_{sys} of about 1 km s^{-1} , which represents an increase by a factor of about 10 compared to the formal fit uncertainty.

3.3.2. Final Rotation Curves

Once the best-fit orientation is determined for a given galaxy, we perform an independent least-squares fit of the velocity field model to the PHANGS–ALMA V_{obs} map to determine the best-fit rotation curve $V_{\text{rot}}(R)$ following the procedure described in Section 3.2.2, but with ϕ , i , and V_{sys} fixed to their best-fit global values. To derive uncertainties, we create 100 realizations of each rotation curve in an iterative process, each time perturbing ϕ , i , and V_{sys} by their respective jackknife error. The center position (X_{cen} , Y_{cen}) is also perturbed by $1''$ in each iteration. The error on rotation velocity at a given radial bin is then computed based on the 16th and 84th percentiles of the 100 realizations. The rotation curves presented and discussed here are based on fits of our first-order model with c_1 determined from harmonic decomposition and all other terms in the expansion set to zero.

For a subset of 15 galaxies (identified and described in Section 4.3), ϕ_{kin} and i_{kin} are significantly affected by imperfect spatial sampling and/or the presence of either strong or spatially extended bars and spirals. In these cases, we adopt the photometric disk inclination i_{phot} to derive the rotation curve.

While the MCMC optimization uses radial bins with width set by the ALMA synthesized beam, our final rotation curves are generated with a fixed 150 pc wide bin in radius, which generates rotation curves that probe a consistent physical scale in all galaxies. This scale is chosen so that it is resolved even for the most distant galaxies (and the bin width corresponds to ~ 1.5 times the median resolution of our data). For many galaxies, this choice has the added advantage of reducing radial variations in the rotation curves that stem from limited spatial sampling of the velocity field. The spatial sampling becomes increasingly inhomogeneous toward large galactocentric radii, which in turn induces correlated structures in our rotation curves. Thus, we eliminate bins where the fraction of detections within a bin falls below a threshold number of pixels. Furthermore, we eliminate bins where the average angular distance of detections from the kinematic major axis exceeds an angle δ . Based on our inspection of the quality of rotational velocity measurements along with the coverage per ring, we adopt $\delta = 55^\circ$ and a 10% threshold for our sample.

4. Results

In this section, we present the results of our modeling technique applied to the high-resolution PHANGS–ALMA CO velocity fields of 67 galaxies. Our assessment of the quality of these results is motivated by extensive testing of the method on mock galaxy velocity fields. These tests confirm the overall accuracy of the method, with the exceptions described in detail in Section 4.2. As a general assessment of the performance of our technique, we find good consistency with a number of kinematic orientations in the literature derived using similar techniques (see Appendix A).

4.1. Example of Results for One Galaxy, NGC 4654

As an example of our results, we highlight the application of our technique to one galaxy, NGC 4654. This galaxy exemplifies the performance of our method on velocity fields with outer clumpy spatial sampling and modest noncircular motions.

Figure 4 shows the observed zeroth- and first-moment map, our best-fit model, and the respective residual field for NGC 4654. The zeroth-moment map compared to the Spitzer $3.6 \mu\text{m}$ image is shown to illustrate the underlying stellar structure of the galaxy relative to the regions sampled by our CO kinematic maps. Further, marginalized PDF posterior distributions for ϕ and i are presented with an indication of the adopted best-fit value and the formal MCMC fit error. For reference, we plot radial profiles of ϕ and i as determined from a tilted-ring analysis with the ROTCUR routine in the Groningen Image Processing System (GIPSY; van der Hulst et al. 1992).

The posterior distributions (middle, bottom) for the global ϕ_{kin} and i_{kin} for NGC 4654 are well sampled and reflect good convergence of the fit. The posterior distributions are typically single peaked and close to Gaussian, but multiple peaks can also occur. In the latter case, the median of the distribution may occasionally fall between the peaks. However, our jackknife uncertainty encompasses the width of the full multi-peaked distribution. These well-behaved posteriors suggest that, despite the presence of noncircular motions, even our most basic model with only circular motion provides a sufficiently good match to the data for obtaining robust global disk orientations. We also note that the posterior distributions of

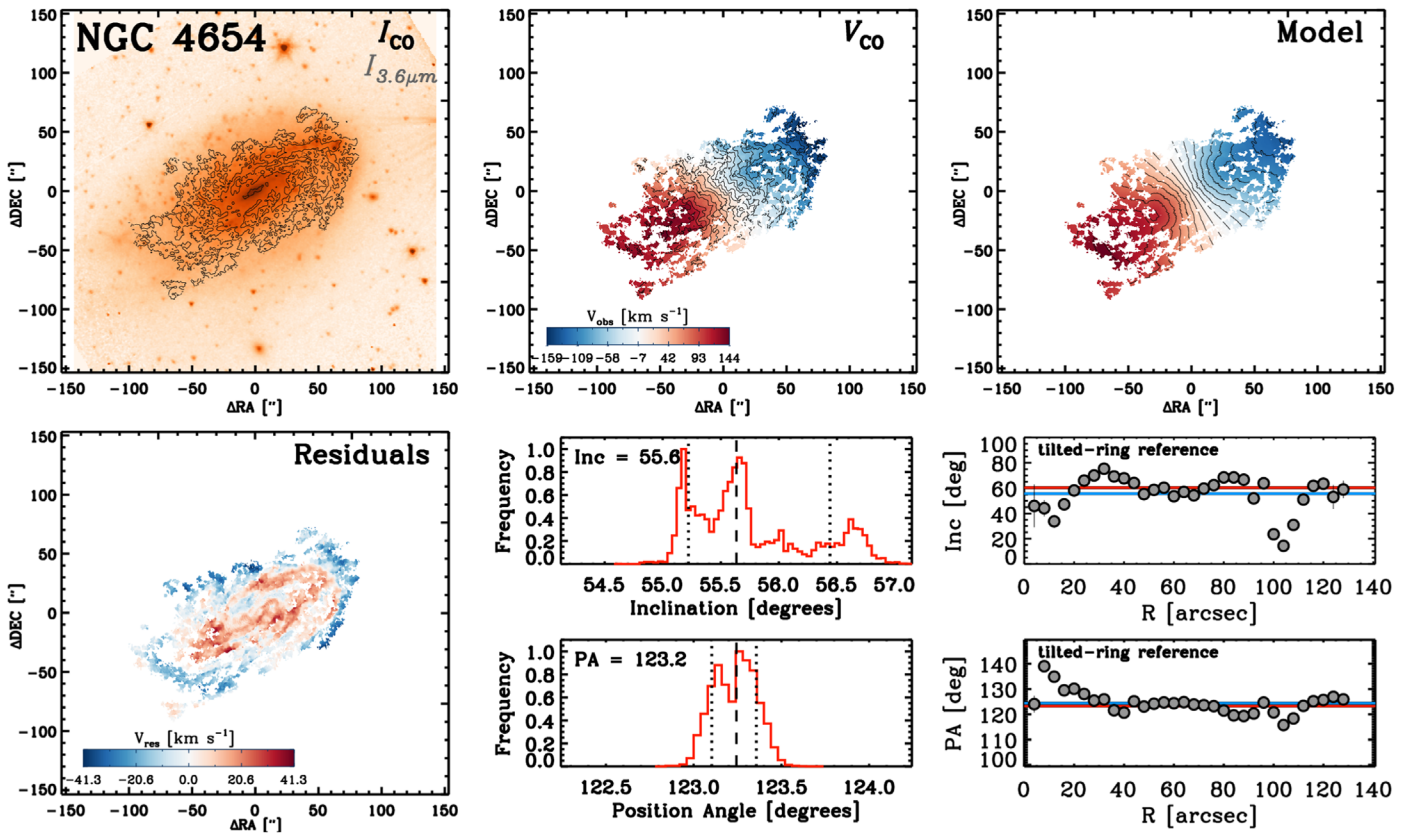


Figure 4. One example case for our modeling results. Top: Spitzer 3.6 μm image with the PHANGS CO contours overlaid, moment 1 velocity field, and best-fit velocity model. Bottom: best-fit residual field with fixed scaling of $\pm 50 \text{ km s}^{-1} \sin(i)$, ϕ and i posterior distributions. The final best-fit inclination i_{kin} and position angle ϕ_{kin} determined from the posterior distributions are indicated as dashed vertical lines, with the 16th and 84th percentiles are shown as vertical dotted lines. Finally, we show the ϕ and i profiles as a function of radius R as inferred from tilted-ring fits to the velocity fields. Our global best fit as well as the median value derived from all tilted rings are indicated by the red and blue horizontal lines, respectively. The best-fit model and residual fields shown are derived from the final orientations ϕ_{kin} and i_{kin} ; note that the latter is replaced by the photometric i_{phot} in case of unreliable fits.

both systemic velocity and excess variance for our fits (not shown) resemble well-sampled Gaussians.

We attribute this behavior to our use of an excess variance term while fitting, which accommodates for differences between the data and fitted model. These differences are apparent in the residual velocity field (bottom left) where the systematic deviations from our model are on the order of $10\text{--}15 \text{ km s}^{-1}$. The excess variance term in this case converges to a similar level.

For NGC 4654, as for the majority of galaxies, nonzero residuals reflect the presence of noncircular motions in the gas not included in our model of pure circular motion. In the specific case of NGC 4654, residuals at radii dominated by the stellar bar ($a_B = 29''$) show in detail the monopolar red–blue pattern characteristic of bars (red along one side, blue along the other; Canzian 1993). At larger radii, the velocity field exhibits the three-armed pattern expected for an $m = 2$ pattern outside corotation (Canzian 1993).

It is worth noting that the structure in the residual velocity map signifies that the observed velocity field is more complex than our chosen model of basic circular motion (rather than that the best-fit model of this kind has not been identified). Nonzero residuals also imply that the global orientation and rotation curve determined with our strategy are not strongly biased by noncircular motions. Alternative strategies that minimize residuals and compensate for noncircular motions by allowing ϕ_{kin} and i_{kin} to unrealistically vary with radius (see the bottom-right two panels of Figure 4, for

example) can yield, on average, an orientation that differs considerably from the global value fitted with our approach. In the case of NGC 4654, the tilted-ring ϕ and i averaged over all radii are consistent with our global solutions, although testing on other galaxies shows that this is sensitive to the area fitted and averaged.

4.2. Overview of Fit Performance and Assessment of Reliability

To assess the reliability of our best-fit parameters, we carefully inspect the performance of each fit with regard to three primary criteria:

- (1) *Physically realistic rotational velocities*—We compare the outermost rotational velocities V_{rot} implied by the deprojected rotation curve associated with the fitted i_{kin} to the velocity implied by the Tully–Fisher relation measured by McGaugh & Schombert (2015) using our integrated stellar mass estimates (Leroy et al. 2020, in preparation). Unreliable fits for the galaxies in our sample (with stellar masses $9.0 < \log M/M_{\odot} < 10.9$) are easily recognizable for their unphysically low ($V_{\text{rot}} < 50 \text{ km s}^{-1}$) or high ($V_{\text{rot}} > 500 \text{ km s}^{-1}$) average deprojected outer rotational velocities. Furthermore, the i_{kin} measured for galaxies with an outer maximum V_{rot} that differs by more than 100 km s^{-1} from the Tully–Fisher value are deemed unreliable.

Table 2
Best-fit Results and Final Orientation Parameters for Our Kinematic Sample

ID	ϕ (deg)	σ_ϕ (deg)	i (deg)	σ_i (deg)	V_{sys} (km s ⁻¹)
IC 1954	63.4	0.2	57.1	0.7	1039.9
IC 5273	234.1	2.0	52.0	2.1	1285.6
NGC 0628	20.7	1.0	8.9	12.2	650.9
NGC 0685	100.9	2.8	23.0	43.4	1347.0
NGC 1087	-0.9	1.2	42.9	3.9	1501.6
NGC 1097*	122.4	3.6	48.6 ^a	6.0	1257.5
NGC 1300*	278.1	0.9	31.8 ^a	6.0	1545.4
NGC 1317	221.5	2.9	23.2	7.7	1930.0
NGC 1365*	201.1	7.5	55.4 ^a	6.0	1613.3
NGC 1385	181.3	4.8	44.0	7.6	1476.7
NGC 1433*	199.7	0.3	28.6 ^a	6.0	1057.4
NGC 1511	297.0	2.1	72.7	1.2	1329.8
NGC 1512*	261.9	4.3	42.5 ^a	6.0	871.4
NGC 1546	147.8	0.4	70.3	0.5	1243.7
NGC 1559	244.5	3.0	65.3	8.4	1275.0
NGC 1566	214.7	4.1	29.6	10.7	1482.5
NGC 1672*	134.3	0.5	42.6 ^b	6.0	1319.2
NGC 1792	318.7	0.8	65.1	1.1	1176.9
NGC 1809	138.2	8.9	57.6	23.6	1288.8
NGC 2090	192.6	0.6	64.5	0.2	897.7
NGC 2283	-4.1	1.0	43.7	3.6	822.1
NGC 2566*	312.3	75.9	48.5 ^a	6.0	1609.6
NGC 2775	156.5	0.1	41.2	0.5	1339.2
NGC 2835	1.0	1.0	41.3	5.3	866.9
NGC 2903	203.7	2.0	66.8	3.1	547.1
NGC 2997	108.1	0.7	33.0	9.0	1076.0
NGC 3059	-14.8	2.9	29.4	11.0	1236.3
NGC 3137	-0.3	0.5	70.3	1.2	1087.1
NGC 3351*	192.7	0.4	45.1 ^a	6.0	774.7
NGC 3507	55.8	1.3	21.7	11.3	969.7
NGC 3511	256.8	0.8	75.1	2.2	1096.7
NGC 3521	343.0	0.6	68.8	0.3	798.1
NGC 3596	78.4	0.9	25.1	11.0	1187.9
NGC 3621	343.7	0.3	65.8	1.8	723.3
NGC 3626*	165.4	0.7	46.6 ^a	6.0	1470.7
NGC 3627	173.1	3.6	57.3	1.0	717.9
NGC 4207	121.9	2.0	64.5	6.0	606.2
NGC 4254	68.1	0.5	34.4	0.9	2388.5
NGC 4293*	46.6	1.1	65.0 ^a	6.0	926.2
NGC 4298	313.9	0.7	59.2	0.7	1137.8
NGC 4303	312.4	2.5	23.5	9.2	1560.2
NGC 4321	156.2	1.7	38.5	2.4	1572.4
NGC 4457*	78.0	1.7	17.4 ^a	6.0	886.0
NGC 4496a	51.1	4.1	53.8	3.5	1722.1
NGC 4535	179.7	1.6	44.7	10.8	1953.1
NGC 4536	305.6	2.3	66.0	2.9	1795.1
NGC 4540	12.8	4.4	28.7	28.7	1286.6
NGC 4548*	136.6	0.5	38.3 ^a	6.0	482.7
NGC 4569*	18.1	4.4	70.0 ^a	6.0	-226.6
NGC 4571	217.5	0.6	32.7	2.1	343.2
NGC 4579	91.3	1.6	40.2	5.6	1516.0
NGC 4654	123.2	1.0	55.6	5.9	1052.6
NGC 4689	164.1	0.2	38.7	2.5	1614.0
NGC 4781	290.0	1.3	59.0	3.9	1248.5
NGC 4826	293.6	1.2	59.1	0.9	409.9
NGC 4941	202.2	0.6	53.4	1.1	1115.9
NGC 4951	91.1	0.5	70.2	2.3	1176.6
NGC 5042	190.6	0.8	49.4	18.1	1386.2
NGC 5068	342.4	3.2	35.7	10.9	667.1
NGC 5134*	308.9	2.8	22.1 ^b	6.0	1749.1
NGC 5248	109.2	3.5	47.4	16.3	1162.0
NGC 5530	305.4	0.9	61.9	2.3	1183.8
NGC 5643*	317.0	2.4	29.9 ^a	6.0	1191.3

Table 2
(Continued)

ID	ϕ (deg)	σ_ϕ (deg)	i (deg)	σ_i (deg)	V_{sys} (km s ⁻¹)
NGC 6300	105.4	2.3	49.6	5.9	1102.2
NGC 6744	14.0	0.2	52.7	2.2	832.4
NGC 7456	16.0	2.9	67.3	4.3	1192.4
NGC 7496	193.7	4.2	35.9	0.9	1636.9

Notes. Galaxies with fits that are deemed unreliable are marked with an asterisk (*).

^a Final inclination adopted from the photometric prior.

^b Final inclination based on the Tully–Fisher relation from McGaugh & Schombert (2015).

- (2) *Reasonable consistency with the galaxy’s photometric appearance*—Galaxies with a salient contrast between the fitted i_{kin} and our i_{phot} prior (with $|i_{\text{kin}} - i_{\text{phot}}| \gtrsim 30$ degrees) are flagged as unreliable.
- (3) *Not strongly affected by large stellar bars*—Galaxies with large strong bars (as quantified by $\epsilon > 0.4$ and $R_{\text{bar}}/R_{\text{CO,max}} \gtrsim 0.45$) are also flagged as unreliable as we find that in those cases our i_{kin} measurements are likely compromised by bar-induced features in the observed velocity field. See Section 4.2.2 for more details.

According to these criteria, we obtain reliable results for the majority (78%) of our kinematic sample. We adopt the best-fit values of ϕ_{kin} and i_{kin} measured with our technique as the final orientation for 52 galaxies in total and use them for all of our subsequent analyses. For all unreliable fit results, we replace our best-fit i_{kin} with our prior i_{phot} when measuring the rotation curve and during all subsequent analysis. We assign an uncertainty of 2° and 6° on ϕ and i , respectively, for these galaxies based on our jackknife analysis (see Section 4.3).

We also perform consistency checks between the rotation velocities implied by i_{phot} and the expectation from the Tully–Fisher relation, and find that for two galaxies in our sample (NGC 1672 and NGC 5134), i_{phot} implies rotational velocities in stark contrast to what is expected from the Tully–Fisher relation. In these cases, we have traced the discrepancy to an issue with the 3.6 μm disk axis ratio used to infer i_{phot} , which seems to be affected by the presence of the outer (pseudo-)ring identified at 3.6 μm in each of these two galaxies (Herrera-Endoqui et al. 2015). Thus, we replace our i_{phot} values with the inclinations that are implied by the McGaugh & Schombert (2015) Tully–Fisher relation, using the total stellar mass and observed projected rotation curve of each of these two galaxies.

For the remaining galaxies, the characteristics of our fit performance vary significantly. The fits that are deemed unreliable according to the above criteria are impacted by the spatial filling of the CO velocity field (see Section 4.2.1; 4 galaxies in total) and/or the presence of a strong nonaxisymmetric bar and/or spiral structure (Section 4.2.2; 11 galaxies in total). Galaxies with problematic fits are flagged in Table 2. Five additional showcases are presented in Appendix B and discussed in detail in the upcoming sections.

4.2.1. Impact of Imperfect Spatial Sampling

The spatial sampling of our data varies significantly across our sample (see Section 2.2) and impacts the coverage of the

mapped velocity field. This can adversely affect the quality of our MCMC fit, depending on how well the major axis information is sampled in the map. When lines of sight close to the minor axis are significantly overrepresented in the PHANGS–ALMA CO velocity field, rotational velocities and orientations are weakly constrained. CO velocity fields with limited radial extents, in which velocities along the major axis never reach the turnover or flat part of the rotation curve, are also compromised.

As an example of how velocity field coverage affects the quality of our MCMC fits, we show the results for NGC 5042 and NGC 4293 in Figure B1. NGC 5042 (top panels) has a covering fraction of 27%, but our fit still yields reliable results given that the coverage is sparse but fairly uniform. The CO emission in NGC 4293 (bottom panels in Figure B1), in contrast, is only detected within the central ~ 2 kpc and, as a result, the rotation curve can only be traced within its inner rising part. The velocity field thus appears like a “solid-body” rotator and the degeneracy between i and V_{rot} in this case prevents reliable measurement of i_{kin} .

4.2.2. Impact of Stellar Bars and Spiral Arms

For galaxies in the sample with especially strong and prominent stellar bars and/or spirals, our fitting technique is unable to reliably measure the disk inclination angle. This is expected, as strong noncircular streaming motions in bars and spiral arms as well as, e.g., gas inflow along bar dust lanes, lead to systematic deviations from our basic model of purely circular motion.

When covering a large fraction of the mapped area (as quantified by $R_{\text{bar}}/R_{\text{CO,max}} \gtrsim 0.45$), strong bars (with $\epsilon > 0.4$) are especially problematic and yield i_{kin} estimates that are unreliable based on our criteria discussed above. We therefore use $R_{\text{bar}}/R_{\text{CO,max}} \gtrsim 0.45$ as a guideline for rejecting kinematic orientations. We emphasize, however, that rejection is, in the end, decided based on detailed inspection of the solution, keeping in mind, e.g., the orientation of the bar with respect to the major axis, the morphology of the gas within the bar, the overall CO filling factor, and the magnitude of streaming motions suggested by the size of velocity residuals. Good kinematic solutions can still be obtained, e.g., for long bars that are oriented along the galaxy major axis, which thus present few strongly biased lines of sight, or when bar orbits are not uniformly populated by gas (given the gas morphology), so that the bar zone contributes only a small fraction of the total number of lines of sight in the velocity field.

The filling factor of the CO outside the bar can also determine the impact of streaming motions from the bar zone on the fitted orientation. Solutions for some systems below our guideline threshold $R_{\text{bar}}/R_{\text{CO,max}} \sim 0.45$ may thus be compromised. However, in our sample, we have found that even when a small bar leads to obvious deviations from circular motion in the observed velocity field, typical CO filling factors are high enough that there are sufficient unbiased lines of sight to obtain an unbiased global fit.

Overall, we find that our technique is able to perform well on the majority of barred systems. Of the 67% of the total sample that is barred, only 11 host the most prominent troublesome bars (see Figure 2). Solutions for these are categorized as bar dominated and flagged as unreliable. Good solutions are obtained for the remaining barred galaxies. As an example, Figure B2 shows the case of NGC 4535 (top panels). Within

the region of the stellar bar ($R_{\text{bar}} = 38''$), strong noncircular motions lead tilted-ring measurements (bottom-right two panels) to deviate strongly from the global best-fit ϕ and i , whereas the outer measured orientation (in bins where the velocity field better traces circular motion) matches the global MCMC fit. In these cases, our ϕ_{kin} and i_{kin} are robust and are only mildly affected by the presence of the bar and/or spiral arms (see Section 4.3).

The results for NGC 5643 (bottom panels in Figure B2) are a good illustration of a failed case, where a prominent stellar bar with strong noncircular motions yields a problematic fit. The failure appears related to the extent of the bar (which reaches 46% of the total CO radial extent) and the high CO covering fraction throughout the bar area.

As an example of the global impact of spiral arms, Figure B3 highlights results for the unbarred galaxy NGC 4254. The CO velocity field covers far out into the disk, reaching radii where the rotation curve flattens out. The noncircular motions associated with the extended spiral arms lead to small apparent deviations in ϕ and i from their global average values. However, as the overall spatial filling factor of the CO velocity field is quite high, the global impact of these narrow features is low, and we are able to obtain a robust MCMC fit.

4.3. Galaxy Orientations

Table 2 lists our final adopted orientation parameters and their associated uncertainties measured with our jackknife analysis, together with our best-fit systemic velocities. For the 15 fits that are deemed unreliable, the i_{kin} measurement is replaced by the respective photometric inclination i_{phot} , indicated in Table 2. We assign a typical uncertainty in those cases (and in cases where we adopt an inclination based on the Tully–Fisher relation) of 6° for i . These values are adopted based on the median jackknife error for our kinematic sample (see Section 3.3.1).

4.3.1. Comparison to Photometric Orientations

Figure 5 compares our kinematic orientations to the photometric orientations throughout the sample. The left panel shows the measurements of i_{kin} and i_{phot} for all galaxies in our sample. The right panel only shows measurements for the subset of 52 galaxies with reliable i_{kin} measurements. Both panels separate barred and unbarred subsets.

Overall, we find good agreement between the kinematic and photometric orientations. The median offsets and scatter based on the 16th and 84th percentiles from a one-to-one relation in both panels of Figure 5 are listed in Table 3.

The basic agreement between the photometric and kinematic orientations implies an underlying consistency between the orientation probed by the CO-emitting disk and the orientation of the outer stellar disk as traced at $3.6 \mu\text{m}$, as considered in more detail in Section 5.1. The agreement suggests that the quality of our fits is robust to variations in the CO filling factor across the sample, except in extreme cases, as discussed in Section 4.2.1.

Furthermore, orientations agree equally well for unbarred and barred galaxies (which show similarly small offsets and scatter in Figure 5 and Table 3). Because the photometric orientations we adopt are largely obtained from the outer disk, this suggests that our kinematics-based ϕ_{kin} are only mildly affected by the presence of bars. The same appears to hold true

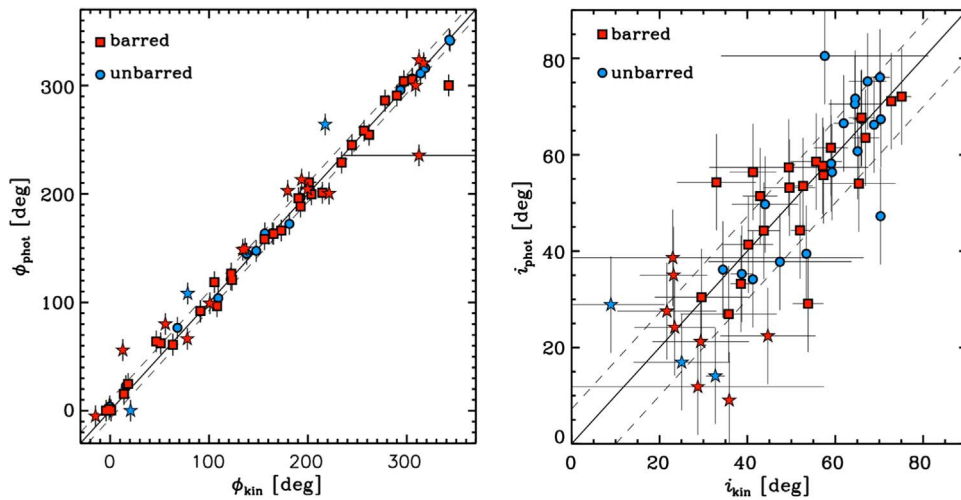


Figure 5. Best-fit position angles ϕ and inclinations i determined from kinematics vs. photometry. We split our sample into barred (red) and unbarred (blue) systems to highlight the impact of bars on measured galaxy orientation. In addition, nearly face-on systems with either i_{kin} or $i_{\text{phot}} < 25^\circ$ are marked with a different symbol. The right panel only includes the subset of 52 galaxies with reliable i_{kin} measurement (see Section 4.2). The error bars shown represent the uncertainties listed in Table 2 and are derived from our jackknife analysis. The solid and dashed lines represent a one-to-one correlation and the scatter in the relations, respectively (see Table 3 for tabulated values).

for our measures of i_{kin} , although the quality of the agreement with i_{phot} is partly biased by our omission of the systems with the most prominent bars (see Section 2.2).

In detail, differences between photometric and kinematic orientations are present, but these can mostly be related to the limitations of our adopted model of uniform galaxy flatness and circularity assumed in Equation (3), as well as the uncertainties inherent at low inclination. Three galaxies have $|\phi_{\text{kin}} - \phi_{\text{phot}}| > 3\sigma$, where σ is the combined uncertainty on the kinematic and photometric angles.²⁴ These are almost exclusively systems with either low i_{kin} or low i_{phot} . For such nearly face-on galaxies that appear nearly circular in projection (axis ratios $\gtrsim 0.75$), the ϕ_{phot} is inherently poorly constrained. At present, however, our adopted errors either on ϕ_{phot} or on i_{phot} represent the average of the differences in inclinations from ellipticities measured in different photometric bands across the sample and therefore do not reflect this systematic trend with inclination.

The systematic disagreement between photometric and kinematic orientations in face-on systems is also evident in the right panel of Figure 5, where the scatter about the one-to-one line increases toward the bottom left of the plot. In a small majority of these nearly face-on cases, i_{phot} underestimates i_{kin} (many systems scatter below the one-to-one relation). This does not appear to be an issue with the fitted i_{kin} , as we find no correlation between the difference $|i_{\text{kin}} - i_{\text{phot}}|$ and most other galaxy properties, including stellar mass, specific star formation rate, R_{25} , B/T, bar presence, bar length, size of the bulge and disk, and fitted rotation curve transition radius r_t . It seems much more likely that the i_{phot} for these systems is biased low, due to a mismatch between the intrinsic flatness of the galaxy and the assumed flatness (with underestimated thickness leading to underestimated i_{phot}), or due to an intrinsic, but modest, departure from circularity in the outer disk shape. These factors, which are discussed more in Section 5.1, introduce discrepancies in i_{phot} that systematically increase in low-inclination systems.

A number of possible physical mechanisms can induce the variations in galaxy shapes that yield discrepant i_{kin} and i_{phot}

Table 3

Median Offsets and Scatter (Taken from the 16th and 84th Percentiles) of the Photometric vs. Kinematic Orientations Presented in Figure 5

Sample	$\langle \phi_{\text{kin}} - \phi_{\text{phot}} \rangle$ (deg)	$\langle i_{\text{kin}} - i_{\text{phot}} \rangle$ (deg)
All	$-1.3^{+7.4}_{-9.9}$	$-0.5^{+10.0}_{-7.2}$
Barred	$-0.9^{+17.6}_{-12.4}$	$-0.6^{+10.4}_{-7.5}$
Unbarred	$-0.7^{+3.5}_{-6.2}$	$1.7^{+7.4}_{-8.5}$

(see Section 5.1). Here we note that, of the few galaxies with $|i_{\text{kin}} - i_{\text{phot}}| > 1\sigma$ and $i_{\text{kin}} > 45^\circ$, the majority are unbarred, making it unlikely that strong noncircular motions are responsible for the offset.

4.3.2. Comparison with Lower-resolution Measurements

Next, we explore the impact of spatial resolution on our orientation measurements. To do so, we repeat our kinematic fits to the PHANGS–ALMA first-moment maps derived from the 7 m (+TP) observations (see A. K. Leroy et al. 2020, in preparation, for details) for the same set of galaxies. These maps are characterized by lower spatial resolution (~ 650 pc on average) and increased surface brightness sensitivity (and thus higher CO covering fraction) compared to our fiducial high-resolution data set. Our comparison of fitted inclinations is restricted to the subset of the sample (44 galaxies) with reliable i_{kin} measured from both the 12 m and 7 m data sets.

In principle, measurements of orientations and rotation curves from fits to lower-angular-resolution velocity fields should be less prone to biases introduced by noncircular motions, which become less prominent with spatial averaging. An increase in beam smearing on the velocity field at lower angular resolution, though, may be expected to affect our ability to constrain the inclination, possibly leading to measurement biases.

In practice, we find that the values we derive for ϕ and i from the 12 m maps are mostly comparable to the values derived from the 7 m data as shown in Figure 6 (and tabulated in Table C1 in Appendix C). For both ϕ and i , we find only small

²⁴ The differences $|i_{\text{kin}} - i_{\text{phot}}|$ are never larger than 3σ .

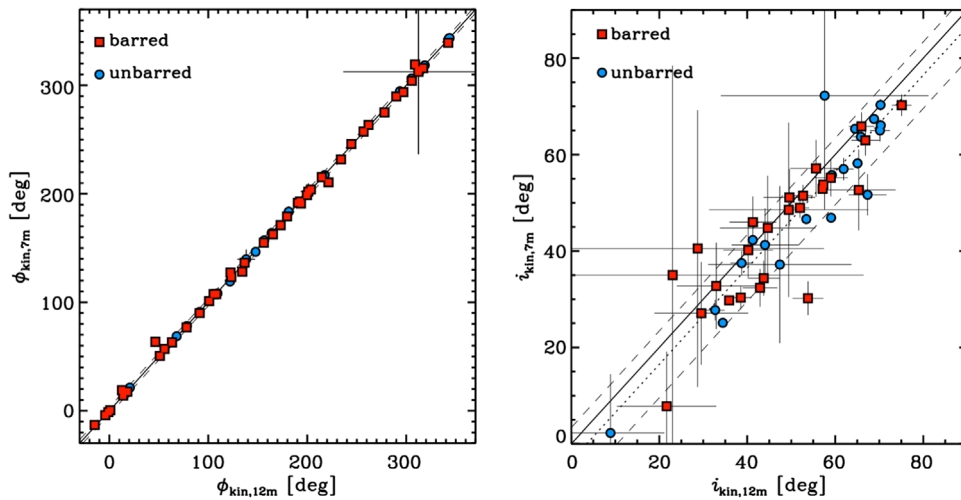


Figure 6. Comparison between the best-fit orientations derived from our 12 m PHANGS–ALMA data set to the same measurements on lower-resolution 7 m ALMA data. Uncertainties are adopted from our jackknife method based on the 12 m data set. Solid, dotted, and dashed lines represent the one-to-one relation, measured offset, and scatter in the relations, respectively. We split our sample into barred and unbarred systems, indicated by red and blue symbols, respectively. The right panel shows the 44 galaxies with reliable i_{kin} measured from both the 12 m and 7 m data sets.

median systematic offsets of $0.0^{+1.0}_{-0.9}$ and $3.5^{+5.8}_{-4.3}$, respectively. The scatter in both relations is in agreement with the uncertainties we have inferred for our measurements.

The tight correspondence between galaxy inclination measured at different spatial resolution highlights the design of our approach, which maximizes constraints from lines of sight not strongly biased by noncircular motions. The small offset to lower inclination when using lower-angular-resolution data plausibly stems from the impact of beam smearing, which not only reduces the inner rotational velocity gradient but also circularizes the distribution of emission. We have found that, with Gaussian smoothing, basic models of projected circular motion are best fit with rings that are systematically less inclined than the adopted inclination by an amount that increases with the size of the Gaussian “beam”. At resolutions typical of the 7 m data, the fitted inclination is lowered by 1° – 4° , which is consistent with the typical offset found in the right panel of Figure 6.

4.4. Rotation Curves

4.4.1. General Characteristics

Figure 7 shows examples of our rotation curves for the set of six galaxies showcased above and in Appendix B. We also present the rotation curves for our full set of 67 galaxies in Appendix D (see Figures D1–D4 as well as Table D1 for all tabulated rotation curves). The error on the inclination dominates the uncertainty on the measured rotation curves. Note that we do not account for bin covariance in our assignment of an uncertainty to each individual radial bin. In each panel, the result of our smooth model fit, performed as described below in Section 4.4.3, is shown for reference. The fitted asymptotic rotation velocity (V_0) and its uncertainty is also reported.

Several key features (typical of the full sample) are evident: first, the CO rotation curve can often be reliably determined out to $\sim 0.7 R_{25}$ (or roughly $\sim 2.2 R_c$; Schruba et al. 2011) and thus captures the characteristic flattening in circular velocity after an initial steep rise. This transition happens on average within $0.1 R_{25}$, according to the rotation curve fits introduced later in

Section 4.4.3. The properties of the inner rotation curve gradient are commented on in Section 5.2.

Many rotation curves exhibit localized wiggles that occur on <500 pc scales (see Henshaw et al. 2020). The smallest of these (5 – 10 km s^{-1}) likely reflect bin-to-bin differences in azimuthal coverage, given the way the morphology of the gas affects the completeness of line-of-sight sampling. Slightly larger wiggles (on the order of 10 – 15 km s^{-1}) may reflect an unaccounted contribution from noncircular motions in spiral arms, which appear on ~ 0.3 – 1 kpc scales, depending on the pitch angle of the spiral.

In obviously barred galaxies, larger wiggles (20 – 40 km s^{-1}) are evident on scales that are consistent with the length of the bar itself. NGC 4535 is a good example (see top panels of Figure B2), where the bar is oriented at $\sim 35^\circ$ with respect to the galaxy’s kinematic major axis, so that noncircular bar-induced streaming motions project strongly into the line of sight. This contributes to the bump in rotational velocity at radii within the bar.

The inner peak in NGC 4535’s rotation curve also reflects a genuine central mass concentration in the form of the inner bulge that occupies the central ~ 1 kpc (Yoshino & Ichikawa 2008). As we will examine in more detail in the next section, the PHANGS CO rotation curves are optimal tracers of central mass concentrations in the sample.

4.4.2. Rotation Curves as Tracers of Galaxy Mass

Figure 8 plots the rotation curves for our full set of 67 galaxies, with the radius normalized by R_{25} . PHANGS–ALMA maps typically extend out to $\sim 0.7 R_{25}$ (or $\sim 2.2 R_c$; Schruba et al. 2011) and the fitted rotation curves regularly trace out to radii where rotational velocities flatten out, thus offering a good view of the enclosed dynamical mass. We see that the amplitude of the outer flat rotational velocity clearly increases with increasing stellar mass. Figure 8 also demonstrates that lower-mass galaxies tend to have more slowly rising rotation curves than higher-mass galaxies and reach lower V_{rot} within $0.2 R_{25}$. These trends in rotation curve shape depending on stellar mass have been observed by, e.g., Kalinova et al. (2017) and are described by global galaxy-scaling relations (Dutton & van den Bosch 2009;

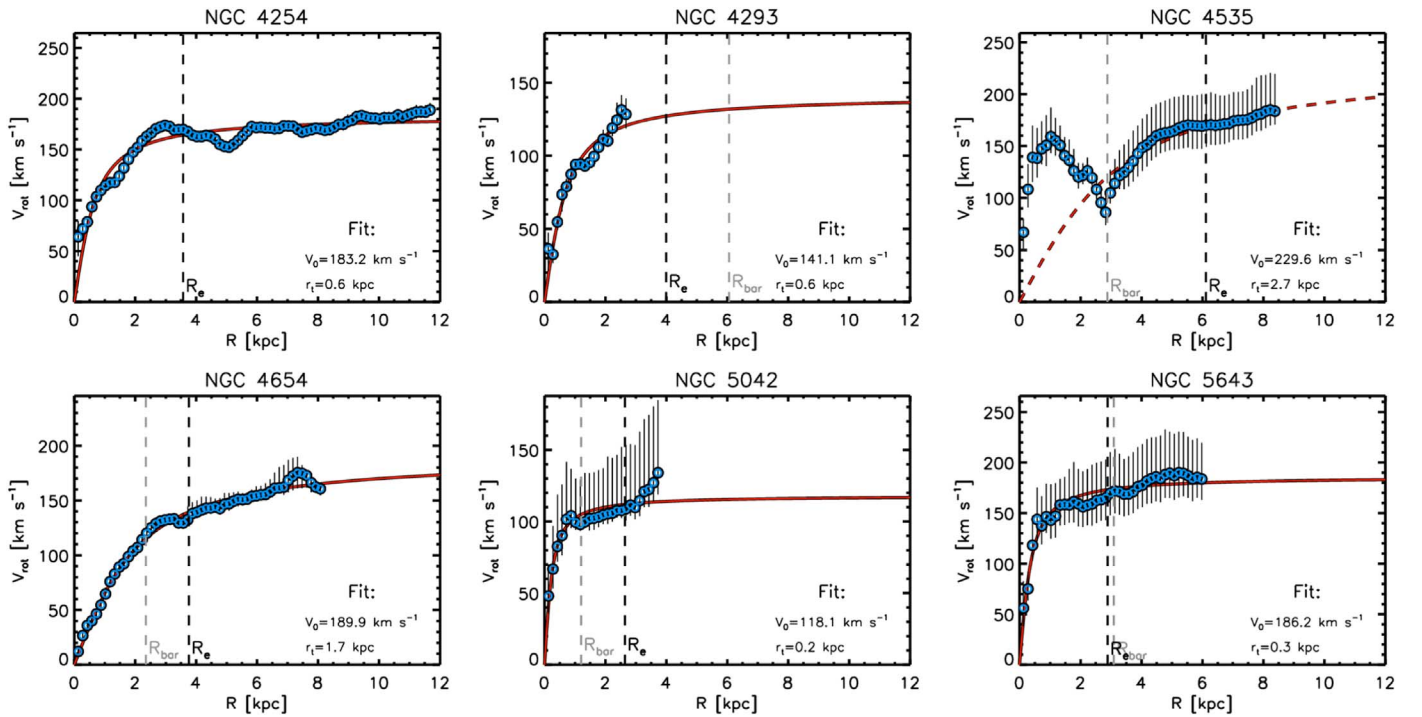


Figure 7. Examples of rotation curves for the subset of galaxies shown in Figure 4 and Appendix B, sampled at a fixed scale of 150 pc. The errors in V_{rot} mainly stem from uncertainties in our orientation parameters. Smooth fits are shown as red lines, together with their best-fit parameters and the asymptotic velocity V_0 . In some panels, the red lines are dashed to indicate cases where the central 2 kpc region have been masked before fitting a smooth model. Effective radii and bar lengths are indicated with dashed vertical lines.

Meidt et al. 2018). We will examine the correlation of the rotation curve shape with stellar mass with the aid of smooth analytic fits further in the next section.

At the innermost radii, rotation curves exhibit a variety of behaviors, particularly in the more massive galaxies in our sample. Given the greater prominence of bulges in more massive systems (e.g., Kormendy & Kennicutt 2004), which is quantified as an increase in bulge-to-total mass ratio (B/T) with increasing stellar mass (see also Bluck et al. 2014), some of the inner behavior appears to trace genuine variation in the mass distribution. In other galaxies, the bar and/or bar-streaming motions may contribute to the recovered rotational velocities. Indeed, prominent bars appear preferentially in the high-mass PHANGS–ALMA targets.

4.4.3. Smooth Analytic Fits

We perform smooth two-parameter analytic fits to the measured rotation curves in the PHANGS–ALMA sample with three main goals. First, we aim to describe the outer asymptotic behavior of the rotation curve, to serve as a guide for modeling circular velocities at and beyond the edge of the CO field of view. The asymptotic behavior is of particular interest for understanding the accuracy with which CO kinematics can be used as a dynamical mass tracer. Second, smooth model fits minimize fluctuations that most likely arise with noncircular motions, rather than track variations in the underlying mass distribution. Thus, smooth analytic fits can be used for fitting the contribution from noncircular motions to the observed velocity field (van de Ven & Fathi 2010; Colombo et al. 2014). The third reason is to obtain a desirable analytical derivative of the rotation curve, as an alternative to the often noisy discrete derivative that can be obtained directly from the measured rotation curve. This is an important quantity when aiming to

quantify the influence of shear on, e.g., molecular cloud evolution (Meidt et al. 2018; Kruijssen et al. 2019; Chevance et al. 2020).

We adopt the empirical parameterization of rotation curves by the function (Courteau 1997)

$$V_{\text{rot}} = V_0 \frac{2}{\pi} \arctan(R/r_t), \quad (10)$$

which describes a smooth rise in rotational velocity up to a maximum V_0 reached asymptotically at infinite radius. The radius r_t denotes the transition between the rising and flat part of the rotation curve and encodes its inner slope. We derive uncertainties on V_0 and r_t by iterating our fits over all 100 Monte Carlo realizations of the rotation curves derived in Section 3.3.2, and then determining the 16th and 84th percentiles of the resulting distributions of V_0 and r_t . In this way, the uncertainties on the fitted parameters are inherited from the uncertainty on the rotation curve itself, which is dominated by the inclination uncertainty. The uncertainty on the asymptotic V_0 is especially sensitive to the inclination uncertainty (while r_t is less so) and, as a consequence, the fractional uncertainties on V_0 are larger at low inclination. Our best-fit V_0 and r_t values are presented in Table 4, together with their uncertainties.

Using these model fits, we compute the velocity at R_{25} , $V_{\text{rot},25}$, and calculate the total dynamical mass within the optical disk via $M_{\text{dyn}, R_{25}} = G^{-1} V_{\text{rot},25}^2 R_{25}$.

For a small fraction of the sample, the inner rotation curve strongly deviates from the basic smooth rise parameterized in Equation (10). This difference tends to be confined to the central ~ 2 kpc (see Figure 8) and marks the influence of central dynamical structures (bulges and bars). Because we are mostly

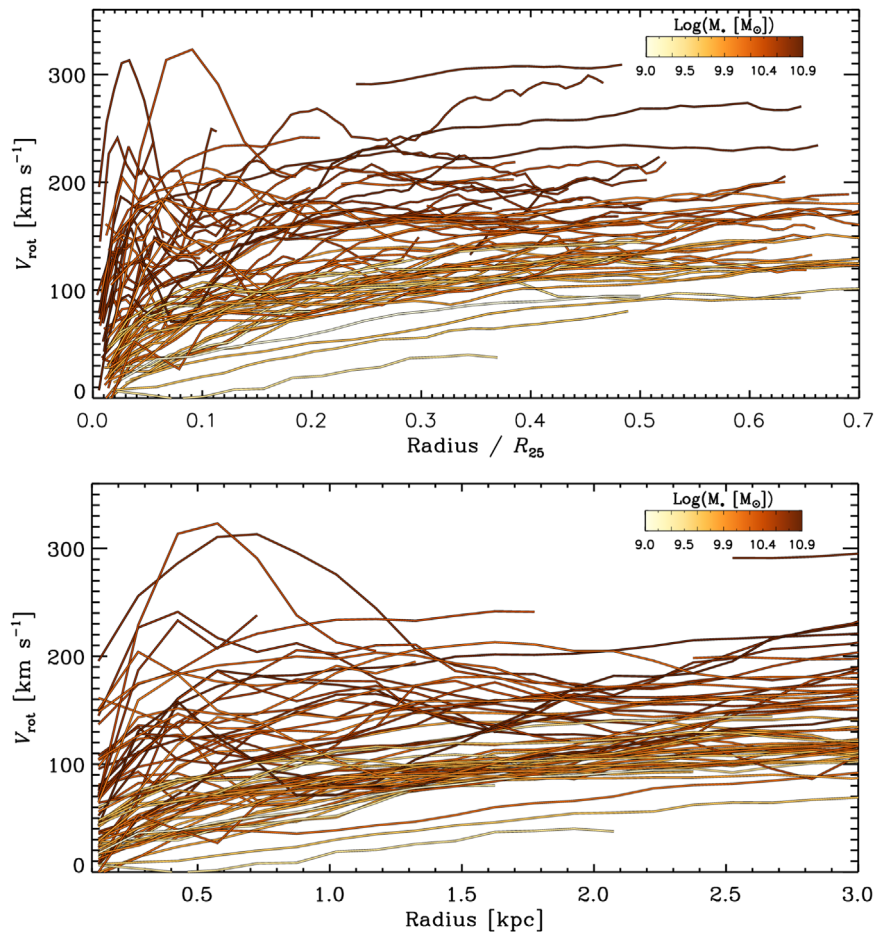


Figure 8. The rotation curves for our sample of 67 galaxies. Top: radii are normalized by R_{25} . Bottom: zoom-in on the inner 3 kpc to highlight the variety of inner rotation curves shapes. The color-coding indicates total stellar mass.

interested in describing the rotation in the disk region, we exclude radii $R < 2$ kpc to prevent this region from dominating our analytic fits. In total, 12 galaxies are masked in this manner, 10 of which are barred.

Galaxies with rotation curves that do not reach beyond $1 R_e$ and/or do not flatten out are not fitted. NGC 2775 and NGC 6744 are also excluded from our smooth fits because rotational velocities could not be measured within the inner galaxy ($\lesssim 2$ kpc) given the morphology of the CO emission (NGC 2775) and the coverage of the ALMA mosaic (NGC 6744). In total, a minor set of six galaxies is excluded from this exercise.

Figure 9 shows the smooth models for the subset of 50 galaxies that have analytic fits, without masking the central $R < 2$ kpc. The figure exhibits a similar sorting by stellar mass present in Figure 8, but now this variation is dominated by the behavior of the rotation curve across the disk-dominated zone. Thus, we see that the mass dependence in the observed rotation curves is only partly driven by the growing prominence of central dynamical structures with increasing galaxy mass.

It is worth emphasizing that for modeling the mass distributions of well-resolved galaxies (and the PHANGS–ALMA sample in particular), the observed rotation curve should be preferred over the smooth model. In this paper, smooth fits most reliably capture only the outer asymptotic behavior and are therefore meant to serve as a guide for

modeling the behavior of the rotation curve at and beyond the edge of the CO field of view.

5. Discussion/Implications

5.1. Galaxy Shapes

Differences in the kinematic and photometric orientations of galaxies can have implications for the intrinsic shapes of their underlying stellar disks. More specifically, our adopted photometric position angles ϕ_{phot} are measured from the projected shape of the outer old stellar disk, whereas the kinematic position angle ϕ_{kin} traces the orientation of the inner disk populated by molecular gas. Small differences could therefore suggest modest twisting of the disk orientation between inner and outer radii. Differences between ϕ_{kin} and ϕ_{phot} may also signify a genuine deviation from disk circularity, as quantified by Franx et al. (1994) and Schoenmakers et al. (1997). Such deviations from perfect disk circularity will have the most notable impact on position angles measured for galaxies at low inclination (although they may still be present to an equal degree in other systems; see discussion below). We note that we find no obvious systematic trend when comparing the offset $\phi_{\text{kin}} - \phi_{\text{phot}}$ against other global galaxy properties (i.e., stellar mass, specific star formation rate, R_{25} , B/T, bar presence, bar length, size of bulge and disk, fitted rotation curve transition radius r_t).

Table 4
Parameters for Smooth Analytic Fits to Our Rotation Curves (see Equation (10))

ID	V_0 (km s ⁻¹)	r_t (kpc)	ID	V_0 (km s ⁻¹)	r_t (kpc)
IC 1954	137.0 ^{+2.9} _{-1.1}	0.69 ^{+0.07} _{-0.04}	NGC 3626	248.8 ^{+33.6} _{-22.3}	0.13 ^{+0.16} _{-0.06}
IC 5273	150.2 ^{+8.5} _{-5.7}	1.30 ^{+0.12} _{-0.11}	NGC 3627	202.1 ^{+6.1} _{-7.3}	0.45 ^{+0.10} _{-0.09}
NGC 0628	144.8 ^{+108.4} _{-37.3}	0.56 ^{+0.05} _{-0.03}	NGC 4207	125.0 ^{+10.1} _{-7.4}	0.93 ^{+0.11} _{-0.09}
NGC 0685	216.8 ^{+119.7} _{-33.2}	1.73 ^{+0.15} _{-0.11}	NGC 4254	183.2 ^{+6.5} _{-4.1}	0.59 ^{+0.07} _{-0.04}
NGC 1087	152.6 ^{+11.5} _{-7.7}	0.35 ^{+0.04} _{-0.02}	NGC 4293	141.1 ^{+15.2} _{-10.2}	0.62 ^{+0.17} _{-0.10}
NGC 1097	328.4 ^{+32.4} _{-26.0}	2.23 ^{+0.43} _{-0.38}	NGC 4298	138.9 ^{+2.7} _{-1.9}	0.81 ^{+0.09} _{-0.06}
NGC 1300	183.3 ^{+45.2} _{-21.6}	0.16 ^{+0.14} _{-0.06}	NGC 4303	178.2 ^{+75.1} _{-43.0}	0.28 ^{+0.14} _{-0.07}
NGC 1317	165.8 ^{+72.9} _{-34.2}	0.18 ^{+0.02} _{-0.03}	NGC 4321	181.0 ^{+9.0} _{-10.5}	0.45 ^{+0.10} _{-0.05}
NGC 1365	186.7 ^{+26.8} _{-18.1}	0.25 ^{+0.20} _{-0.13}	NGC 4457
NGC 1385	136.6 ^{+17.8} _{-9.2}	0.50 ^{+0.10} _{-0.07}	NGC 4496a	136.9 ^{+13.3} _{-7.0}	2.85 ^{+0.23} _{-0.23}
NGC 1433	204.5 ^{+43.3} _{-27.9}	0.59 ^{+0.02} _{-0.02}	NGC 4535	229.6 ^{+44.4} _{-34.9}	2.67 ^{+0.20} _{-0.41}
NGC 1511	228.7 ^{+17.6} _{-14.6}	2.63 ^{+0.37} _{-0.28}	NGC 4536	170.9 ^{+3.9} _{-2.4}	0.06 ^{+0.06} _{-0.03}
NGC 1512	178.9 ^{+20.1} _{-15.1}	0.15 ^{+0.04} _{-0.03}	NGC 4540	164.3 ^{+108.7} _{-42.3}	1.09 ^{+0.32} _{-0.20}
NGC 1546	180.0 ^{+2.5} _{-1.3}	0.36 ^{+0.06} _{-0.03}	NGC 4548	192.9 ^{+23.1} _{-14.8}	0.07 ^{+0.03} _{-0.01}
NGC 1559	237.0 ^{+37.0} _{-22.0}	4.01 ^{+1.26} _{-0.67}	NGC 4569	273.5 ^{+20.6} _{-23.4}	2.89 ^{+0.50} _{-0.46}
NGC 1566	220.6 ^{+105.9} _{-54.4}	0.00 ^{+0.16} _{-0.00}	NGC 4571	137.1 ^{+7.8} _{-5.2}	0.63 ^{+0.04} _{-0.02}
NGC 1672	160.4 ^{+45.3} _{-26.5}	1.15 ^{+0.32} _{-0.27}	NGC 4579	314.0 ^{+43.3} _{-28.8}	1.50 ^{+0.09} _{-0.10}
NGC 1792	179.4 ^{+2.5} _{-1.3}	0.92 ^{+0.10} _{-0.06}	NGC 4654	189.9 ^{+8.5} _{-6.5}	1.67 ^{+0.05} _{-0.03}
NGC 1809	NGC 4689	150.6 ^{+9.7} _{-6.2}	0.83 ^{+0.06} _{-0.03}
NGC 2090	176.9 ^{+3.4} _{-2.9}	0.42 ^{+0.06} _{-0.04}	NGC 4781	127.5 ^{+3.6} _{-2.8}	0.65 ^{+0.05} _{-0.04}
NGC 2283	114.2 ^{+6.6} _{-3.8}	0.37 ^{+0.02} _{-0.01}	NGC 4826	189.9 ^{+1.7} _{-1.3}	0.04 ^{+0.01} _{-0.01}
NGC 2566	166.7 ^{+28.4} _{-43.2}	0.21 ^{+0.31} _{-0.21}	NGC 4941	232.0 ^{+2.7} _{-1.7}	1.62 ^{+0.04} _{-0.04}
NGC 2775	NGC 4951	137.8 ^{+7.9} _{-4.2}	0.38 ^{+0.09} _{-0.07}
NGC 2835	NGC 5042	118.1 ^{+45.6} _{-6.8}	0.21 ^{+0.04} _{-0.03}
NGC 2903	309.8 ^{+12.7} _{-6.3}	2.49 ^{+0.23} _{-0.14}	NGC 5068
NGC 2997	210.2 ^{+52.2} _{-23.0}	0.17 ^{+0.04} _{-0.02}	NGC 5134	210.1 ^{+72.7} _{-38.4}	2.17 ^{+0.55} _{-0.42}
NGC 3059	139.3 ^{+54.2} _{-21.9}	0.72 ^{+0.13} _{-0.08}	NGC 5248	196.5 ^{+67.9} _{-26.4}	1.02 ^{+0.34} _{-0.36}
NGC 3137	130.7 ^{+2.7} _{-2.3}	0.94 ^{+0.08} _{-0.05}	NGC 5530	153.7 ^{+1.6} _{-1.4}	1.11 ^{+0.03} _{-0.02}
NGC 3351	206.8 ^{+16.9} _{-13.9}	0.30 ^{+0.08} _{-0.03}	NGC 5643	186.2 ^{+40.8} _{-23.2}	0.32 ^{+0.04} _{-0.03}
NGC 3507	180.9 ^{+108.6} _{-61.0}	0.44 ^{+0.08} _{-0.02}	NGC 6300	199.3 ^{+24.8} _{-13.3}	0.66 ^{+0.20} _{-0.12}
NGC 3511	133.2 ^{+4.7} _{-2.2}	0.33 ^{+0.07} _{-0.04}	NGC 6744
NGC 3521	236.8 ^{+0.7} _{-1.0}	0.32 ^{+0.02} _{-0.02}	NGC 7456	121.0 ^{+2.3} _{-2.0}	0.84 ^{+0.06} _{-0.04}
NGC 3596	151.9 ^{+99.6} _{-34.9}	0.38 ^{+0.06} _{-0.03}	NGC 7496	147.7 ^{+4.8} _{-5.6}	1.92 ^{+0.12} _{-0.12}

Offsets in photometric and kinematic inclinations may likewise indicate a genuine change in the underlying disk structure, in particular the variation of the inclination between the inner disk (traced by CO kinematics) and the outer disk (traced at 3.6 μm), i.e., warping. Such warping might arise as part of the same gravitational response that is thought to generate the more readily recognizable outer HI warps of galaxies (Sellwood 2010; see also Rogstad et al. 1974; Briggs 1990). We find no evidence of residual correlation between $|i_{\text{phot}} - i_{\text{kin}}|$ and many other global galaxy properties (see list above).

Interestingly, the lack of a strong correlation with stellar mass suggests that large differences $|i_{\text{phot}} - i_{\text{kin}}|$ are not related to systematic variations in disk flatness, which is another source of discrepancy between i_{phot} and i_{kin} . This may offer an interesting contrast to the increase in light-weighted flatness with increasing mass found by Yoachim & Dalcanton (2006) across a broader mass range than studied here, perhaps signifying the growing prominence of a thin disk component with increasing mass.

Any variations from the constant flatness assumed in Equation (3) (in the range 0.1–0.4 over the mass range

analyzed in this paper; van der Wel et al. 2014) appear more likely to be a source of scatter between i_{phot} and i_{kin} (i.e., as plotted in Figure 5); any individual galaxy may still reflect departures of the true thickness from the specific value we have adopted. Scatter in inclinations may also arise as a result of variations in disk circularity. We emphasize, though, that variations in thickness and/or circularity may be likely to introduce systematic discrepancies, such as highlighted at low inclination in Section 4.3.1. This is due to the fact that only modest variations in these shape parameters can cause large discrepancies for face-on systems. We estimate that, with our adopted flatness $q = 0.25$, when $i < 25^\circ$, the inferred inclination will increase by 20° with an increase in axis ratio by as little as 0.1, whereas for $i > 45^\circ$, this change to the inclination corresponds to a much larger change ($\gtrsim 0.2$) in the axis ratio.

5.2. Inner Rotation Curve Shapes at High Resolution as Tracers of the Central Mass Distributions of Galaxies

In Section 4.4.1, we identified a variety of inner rotation curve shapes throughout the PHANGS–ALMA sample. Here, we consider whether the central rotation curve is shaped by a genuine central mass concentration or by a lingering

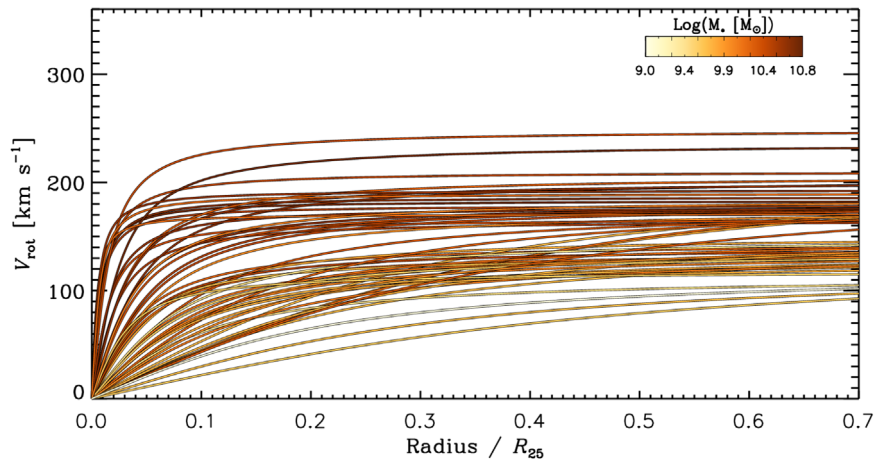


Figure 9. Smooth model fits to the rotation curves, with radii normalized to R_{25} . The color-coding indicates the total stellar mass. Shown is the subset of 50 galaxies with robust analytic fits and where the central 2 kpc have not been masked.

contribution from noncircular motions in bars. We do so by quantifying the inner rotation curve gradient of all galaxies and examining whether these gradients are linked with independent measurements of the central mass concentration. Figure 10 plots the linear slope measured between $R = 0$ and $R = 500$ pc of our rotation curves against galaxy stellar mass. Shown are all galaxies except for NGC 2775 and NGC 6744, whose rotation curves do not cover the central regions.

Overall, we find a good correlation between the inner rotation curve slope and total stellar mass (with a Spearman’s rank correlation coefficient of 0.63). This is consistent with the well-known dependency of the inner galaxy structure (i.e., inner bar and bulge components) and total stellar mass (Kormendy & Kennicutt 2004; Bluck et al. 2014), and suggests that our high-resolution curves are good probes of the inner mass distributions of galaxies. To further disentangle the correlation of stellar mass and inner structure, each galaxy is shown color-coded by the stellar mass ratio of the bulge component with respect to the total galaxy, B/T, measured by Salo et al. (2015) within S⁴G. (We note that the bulge component measured by Salo et al. 2015 reflects a genuine central mass concentration and not a bar component, which is fitted independently in their analysis.) To highlight the potential influence of the noncircular orbital structure of bars on our measured inner rotation curves, we furthermore split the sample into barred and unbarred systems.

Together with the expected increase in B/T with stellar mass (e.g., Bluck et al. 2014), Figure 10 also clearly shows an increase in rotation curve slope with B/T at fixed stellar mass: galaxies with the most pronounced bulges exhibit the steepest inner rotation curves. Correlating B/T with our rotation curve slope estimates yields a Spearman’s rank correlation coefficient of 0.60. The correlation of rotation curve slope and stellar mass does not seem to be strongly affected by bar components as barred and unbarred galaxies fall into the same locus of parameter space in Figure 10.

To further examine the correspondence between the inner structure in our high-resolution CO rotation curves and the central mass distributions, we show the inferred inner (≤ 500 pc) dynamical mass versus the stellar mass within the same radius in Figure 11. The dynamical mass is calculated according to $M_{\text{dyn}} = G^{-1} V_{\text{rot}}^2 R$, evaluated at $R = 500$ pc, assuming a spherical geometry. We expect this mass to be dominated by the stellar component at these radii. To obtain an

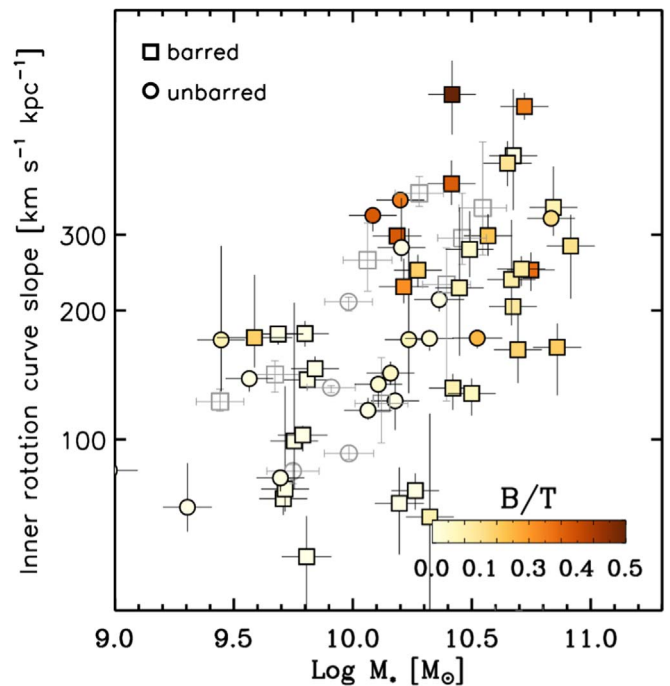


Figure 10. Inner (≤ 500 pc) rotation curve slope plotted against total stellar mass. Squares and circles represent barred and unbarred galaxies, respectively. The color-coding encodes the B/T ratio taken from Salo et al. (2015). Gray symbols represent systems with no B/T measurement. Galaxies with unconstrained inner rotation curves (NGC 2775, NGC 6744) are omitted.

independent measure of this enclosed stellar mass, we determine the fraction of the total $3.6 \mu\text{m}$ emission arising from within the central 500 pc using the S⁴G Sérsic models fitted by Salo et al. (2015), and then multiply this fraction by our fiducial total stellar mass estimates (Section 2.1). Thus, only the S⁴G subset of our sample is shown in Figure 11.

Overall, the two mass estimates track each other fairly well, although there is a significant degree of scatter, most of which can be credited to various sources of systematic uncertainty that are not accounted for in making this coarse comparison. This includes distance uncertainties, for example, and the adopted $3.6 \mu\text{m}$ mass-to-light ratio, which we have assumed is global (thus ignoring local changes in the properties of the stellar population and the amount of contamination by dust emission;

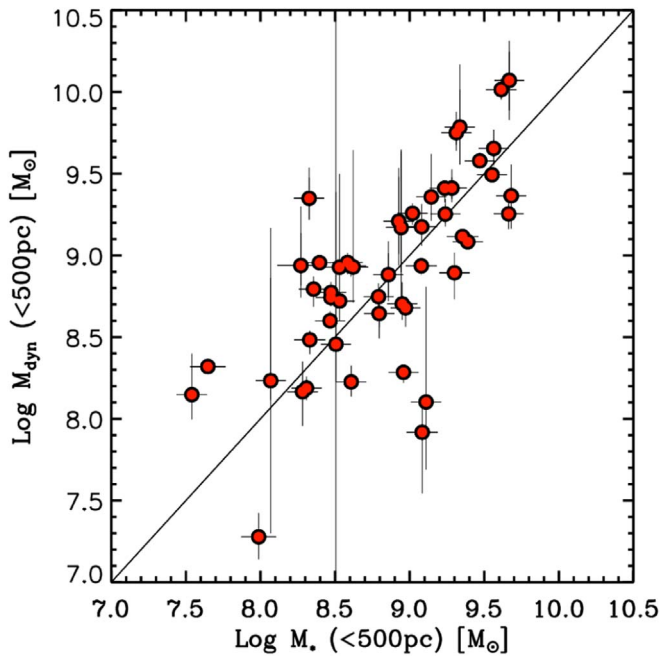


Figure 11. Inner dynamical mass vs. stellar mass inside radii ≤ 500 pc. The solid line marks a one-to-one relation. Shown are 51 galaxies that are covered by S⁴G, excluding galaxies with unconstrained inner rotation curves (NGC 2775, NGC 6744).

e.g., see Querejeta et al. 2015; Leroy et al. 2019). A decrease in the central M/L as a result of enhanced dust emission in the $3.6 \mu\text{m}$ band would lower M_* (< 500 pc) in many of the cases with unrealistic $M_* > M_{\text{dyn}}$, for example. Instances where M_{dyn} (< 500 pc) exceeds M_* (< 500 pc), on the other hand, likely indicate either that the central enclosed mass distribution is flatter than assumed or that the mass in gas is not negligible.

Even with the coarseness of the approximations adopted in Figure 11, we can recognize that the two mass estimates are reassuringly similar. We find a median ratio $\langle \log M_{\text{dyn}}/M_\odot - \log M_*/M_\odot \rangle = 0.1_{-0.4}^{+0.3}$, where the quoted errors quantify the scatter based on the 16th and 84th percentiles. The correlation coefficient of the relation is 0.73.

5.3. Rotational Velocities as Tracers of Global Mass: the Tully–Fisher Relation

We now examine the degree to which our high-resolution CO kinematics trace global dynamical mass, using the stellar mass Tully–Fisher relation (Tully & Fisher 1977) as our point of reference (see also Leung et al. 2018 for an evaluation of dynamical mass estimation relative to CO kinematics).

The Tully–Fisher relation implies a tight fundamental relation between rotation velocity and total stellar mass. Figure 12 shows the Tully–Fisher relation for our sample using the outer rotational velocities $V_{\text{rot},25}$ estimated by extrapolating our CO rotation curves out to R_{25} using our fitted smooth arc tangent models. The stellar Tully–Fisher relation recently measured in massive spiral galaxies in the local universe by McGaugh & Schombert (2015) is also shown. Note that galaxies without robust smooth fits are omitted. Also, the $V_{\text{rot},25}$ in this plot are derived from rotation curves that assume a mix of kinematic and photometric inclinations. Thus, the plotted values do not include outer V_{rot} measurements from the problematic fits (described in Section 4.2) that yield

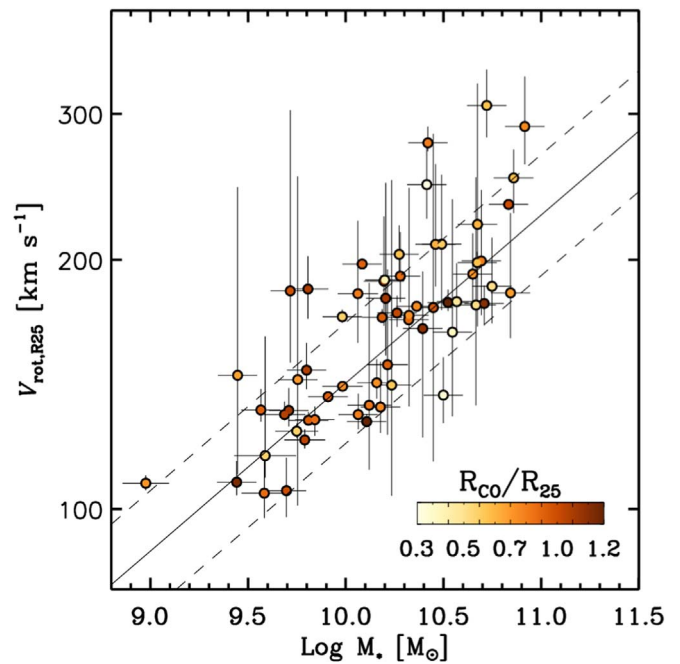


Figure 12. Tully–Fisher relation, based on total stellar masses and outer rotation velocities ($V_{\text{rot},25}$) of our galaxy sample. Rotation velocities are derived from our smooth analytic fits to rotation curves. The color-coding encodes the radial coverage of CO relative to the size of the optical disk. The solid and dashed lines show the stellar Tully–Fisher relation and its scatter from McGaugh & Schombert (2015), respectively. Only systems with robust kinematic fits are shown (52 galaxies).

unreliable i_{kin} values and more than 100 km s^{-1} difference between the outer V_{rot} and the Tully–Fisher value; instead, the plot shows the $V_{\text{rot},25}$ fitted to the rotation curve at the adopted i_{phot} .

The correlation recovered in Figure 12, albeit with substantial scatter, suggests that the inner kinematics probed in our PHANGS–ALMA CO maps provide reasonably good constraints on the asymptotic behavior of rotation curves. The scatter in our reconstructions of $V_{\text{rot},25}$ at fixed stellar mass is ~ 0.07 dex.

The measurements in Figure 12 largely fall within the scatter around the stellar Tully–Fisher relation measured by McGaugh & Schombert (2015). We refer the reader to their discussion of the uncertainties responsible for this scatter, as they are expected to contribute similarly here. An additional potential source of scatter is related to the extent that CO kinematics from the inner disk can be extrapolated to large radii. The color-coding of the data points in Figure 12 shows the fraction of the optical extent of the disk covered by CO emission. We find no significant relation between the scatter about the Tully–Fisher relation and the extent of the mapped area for the galaxies in our sample. This emphasizes that the kinematics contained in CO maps with even limited radial coverage can provide constraints on the kinematics beyond the mapped edge using our smooth two-parameter model.

6. Summary and Conclusions

In this work, we have introduced a novel method to constrain disk orientations and rotation curves for 67 galaxies with sensitive, high-resolution CO(2–1) observations from the PHANGS–ALMA survey of local star-forming galaxies. This

has allowed us to systematically constrain the detailed shapes of rotation curves at 150 pc resolution across a wide range of galaxy properties. Our main results are the following:

1. Our methodology for constraining disk position angles and inclination angles utilizes all sampled lines of sight in a given velocity field, making it well-suited for high-spatial-resolution CO maps that can have a low area filling factor.
2. Our approach affords limited sensitivity to nonaxisymmetric dynamical structures, which are common features in the central regions of galactic disks probed by CO emission. In general, we find good agreement (within 3σ) between our kinematics-based galaxy orientations and those inferred from outer disk photometry, implying that the impact of stellar bars and spirals on our derived orientations is very limited, except in the most prominently barred cases. For face-on disks, where the photometric position angle can be ill-constrained, our kinematics position angles yield a visibly better description of the CO kinematics.
3. We derive galaxy rotation curves across the PHANGS–ALMA sample by fitting a basic model of pure circular motion to each observed velocity field. These typically extend out to $\sim 0.7 R_{25}$ and exhibit qualities that correlate with other galaxy properties. We find that the inner velocity gradient increases with both stellar mass and bulge prominence, for example.
4. We introduce smooth analytic models of our rotation curves and use these to demonstrate that CO rotational velocities hold promise as tracers of both inner dynamical mass and global dynamical mass, once several systematics (mass-to-light ratio variations, stellar geometry/distribution) can be accounted for.
5. The flexibility of our technique for deriving galaxy orientations and rotation curves makes it well-suited for a variety of future applications. This includes higher-order velocity field decompositions that can be used to constrain noncircular gas motions and inflows. Our method can also be applied to velocity fields constructed from optical emission and/or absorption-line tracers, as well as HI emission.

The measurements presented in this paper form the basis for a wealth of future studies, including tests of the maximum disk hypothesis (and/or constraints on galaxy dark matter fractions) with detailed dynamical modeling and comparisons between global mass estimates via unresolved kinematics versus highly resolved rotation curves.

This work was carried out as part of the PHANGS collaboration. The authors acknowledge fruitful discussions with Arjen van der Wel and Erwin de Blok. P.L., E.S., C.F., and D.L. acknowledge support from the European Research Council (ERC) under the European Union’s Horizon 2020 research and innovation program (grant agreement No. 694343). E.R. acknowledges the support of the Natural Sciences and Engineering Research Council of Canada (NSERC), funding reference number RGPIN-2017-03987. J.M.D.K. and M.C. gratefully acknowledge funding from the Deutsche Forschungsgemeinschaft (DFG) through an Emmy Noether Research Group (grant No. KR4801/1-1) and the DFG Sachbeihilfe (grant No. KR4801/2-1). J.M.D.K. gratefully acknowledges funding from the European Research Council

(ERC) under the European Union’s Horizon 2020 research and innovation program via the ERC Starting Grant MUSTANG (grant agreement No. 714907). S.C.O.G. acknowledges support from the Deutsche Forschungsgemeinschaft via SFB 881 “The Milky Way System” (Project-ID 138713538; subprojects B1, B2, and B8) and via Germany’s Excellence Strategy EXC 2181/1-390900948 (the Heidelberg STRUCTURES Excellence Cluster). C.H., A.H., and J.P. acknowledge support from the Programme National “Physique et Chimie du Milieu Interstellaire” (PCMI) of CNRS/INSU with INC/INP co-funded by CEA and CNES, and from the Programme National Cosmology and Galaxies (PNCG) of CNRS/INSU with INP and IN2P3, co-funded by CEA and CNES. J.P. and F.B. acknowledge funding from the European Union’s Horizon 2020 research and innovation program (grant agreement No. 726384).

This paper makes use of the following ALMA data: ADS/JAO.ALMA#2013.1.00650.S; #2013.1.00803.S; #2013.1.01161.S; #2015.1.00925; #2015.1.00956; #2017.1.00392.S; #2017.1.00886.L; and #2018.1.01651.S. ALMA is a partnership of ESO (representing its member states), NSF (USA) and NINS (Japan), together with NRC (Canada), MOST and ASIAA (Taiwan), and KASI (Republic of Korea), in cooperation with the Republic of Chile. The Joint ALMA Observatory is operated by ESO, AUI/NRAO and NAOJ. The National Radio Astronomy Observatory is a facility of the National Science Foundation operated under cooperative agreement by Associated Universities, Inc. We acknowledge the use of the Extragalactic Distance Database (Tully et al. 2009), the HyperLeda database (Makarov et al. 2014), and the NASA/IPAC Extragalactic Database.

Appendix A Consistency between the Kinematic Orientations Fitted in This Work and Independently Derived Values

In this appendix, we provide a sense of the basic consistency between the orientations fitted with the approach developed here and alternative methods used in the literature. To date, an abundance of kinematics surveys have yielded quality measurements of the position angle, inclination angle, and rotation curves using techniques similar to ours. These offer the potential to examine the impact of differences in fitting strategy on the fitted kinematic parameters. For now, given that the overlap between these surveys and PHANGS–ALMA targets is quite small (summarized below), the comparison we draw here mostly offers a confirmation of consistency between approaches.

In what follows we will consider only comparisons between kinematics orientations and defer a comparison of rotation curves to future work. This is as we expect measured rotation curves to be sensitive to the choice of tilted-ring fitter as well as the resolution of the kinematic tracer and the nature of its true three-dimensional organization (given variations in intrinsic velocity dispersion, vertical distribution, and relation to structure in the disk plane; as highlighted recently by Levy et al. 2018, 2019, and Colombo et al. 2014).

Our PHANGS–ALMA sample has two galaxies in common with the GHASP survey modeled by Epinat et al. (2008; NGC 2775 and NGC 3596), two galaxies in common with SPARC (NGC 2903 and NGC 3521; Lelli et al. 2016), six galaxies in common with the HI sample modeled by Ponomareva et al. (2016; NGC 1365, NGC 3351, NGC 3621, NGC 3627, NGC 4535, and NGC 4536), and five galaxies from THINGS with tilted-ring fitted orientations (but no tabulated uncertainties; see de Blok et al. 2008; NGC 2903, NGC 3521, NGC 3621, NGC 3627, and NGC 4826). An additional 14 galaxies covered

by VIVA (NGC 4254, NGC 4293, NGC 4298, NGC 4321, NGC 4424, NGC 4457, NGC 4535, NGC 4536, NGC 4548, NGC 4569, NGC 4579, NGC 4654, NGC 4689, and NGC 4694; see Chung et al. 2009) have not yet had their HI velocity fields modeled.²⁵

In the majority of these cases, the orientations determined by fitting to CO velocity fields are consistent with the published kinematic orientations within the published uncertainties, where tabulated. Orientations for the galaxies in GHASP and SPARC (which tend to have larger uncertainties σ_{lit} than the uncertainties σ fitted in this work) are less than $1\sigma_{\text{lit}}$ different from our orientations. The uncertainties on the orientations modeled by Ponomareva et al. (2016) are more similar to our uncertainties. For this subset of galaxies, agreement is within 1.5σ on average.

With two exceptions, our orientations are also largely consistent (within 1.5σ) with those published by de Blok et al. (2008)

using our uncertainties on both position angle and inclination to measure agreement (given that the uncertainties associated with the values from de Blok et al. are not published). For two galaxies (NGC 3521 and NGC 4826) where our inclination differs by more than 2σ from the THINGS value, we have found that our CO kinematical orientation agrees very well with the $3.6\ \mu\text{m}$ photometric orientation. For one of these, NGC 4826, the position angles also differ substantially. This stems from a well-known kinematic decoupling between the central 1 kpc traced by CO and the extended disk probed by HI (Casoli & Gerin 1993).

Appendix B MCMC Fit Examples

Here we showcase the performance of our fitting on five galaxies (Figures B1–B3) as discussed in Section 4.

²⁵ For this subset, only photometric orientations were tabulated by Chung et al. (2009).

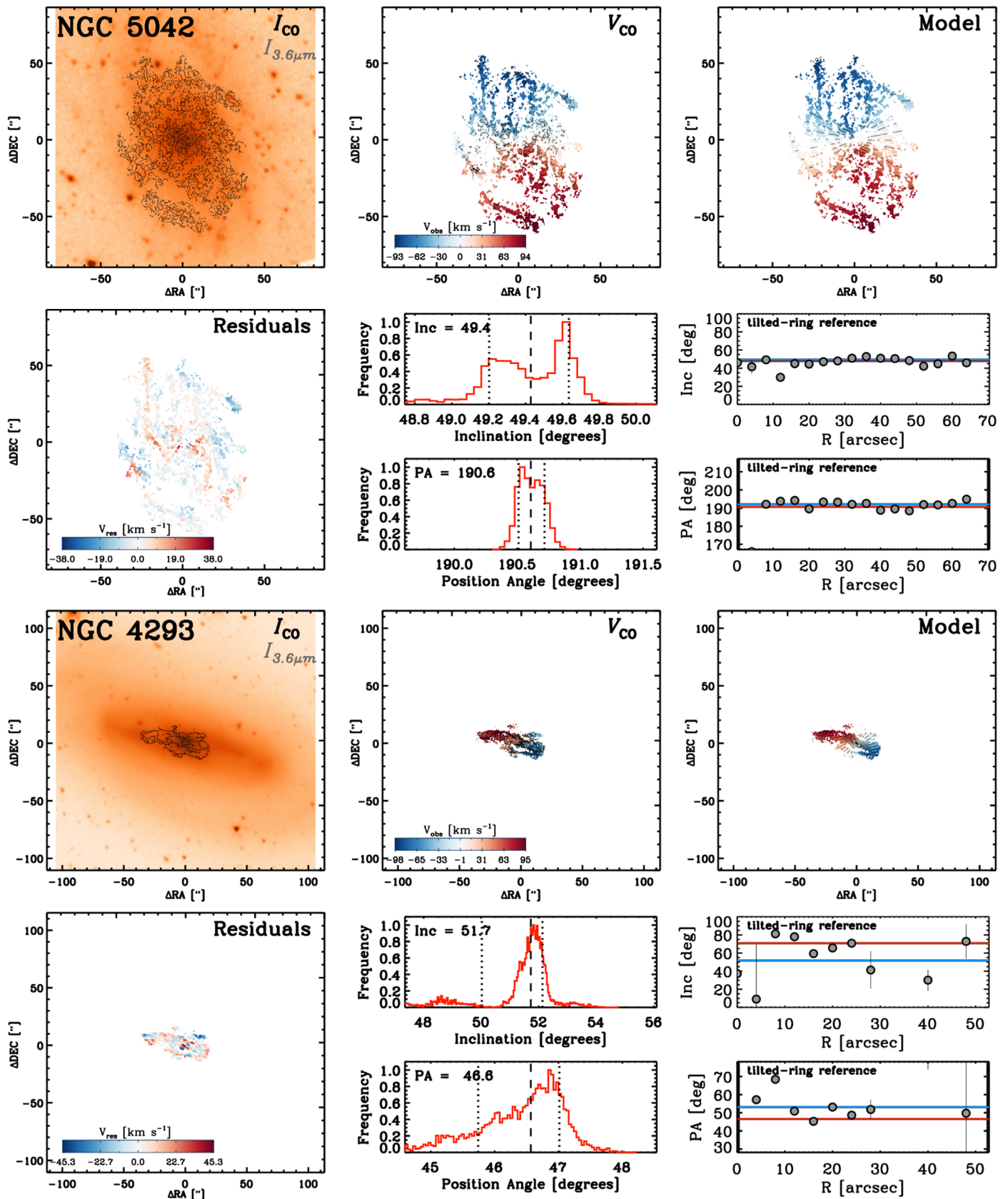


Figure B1. Same as Figure 4, but showing two additional example galaxies to highlight the effect of variations in spatial sampling on our kinematic fit performance.

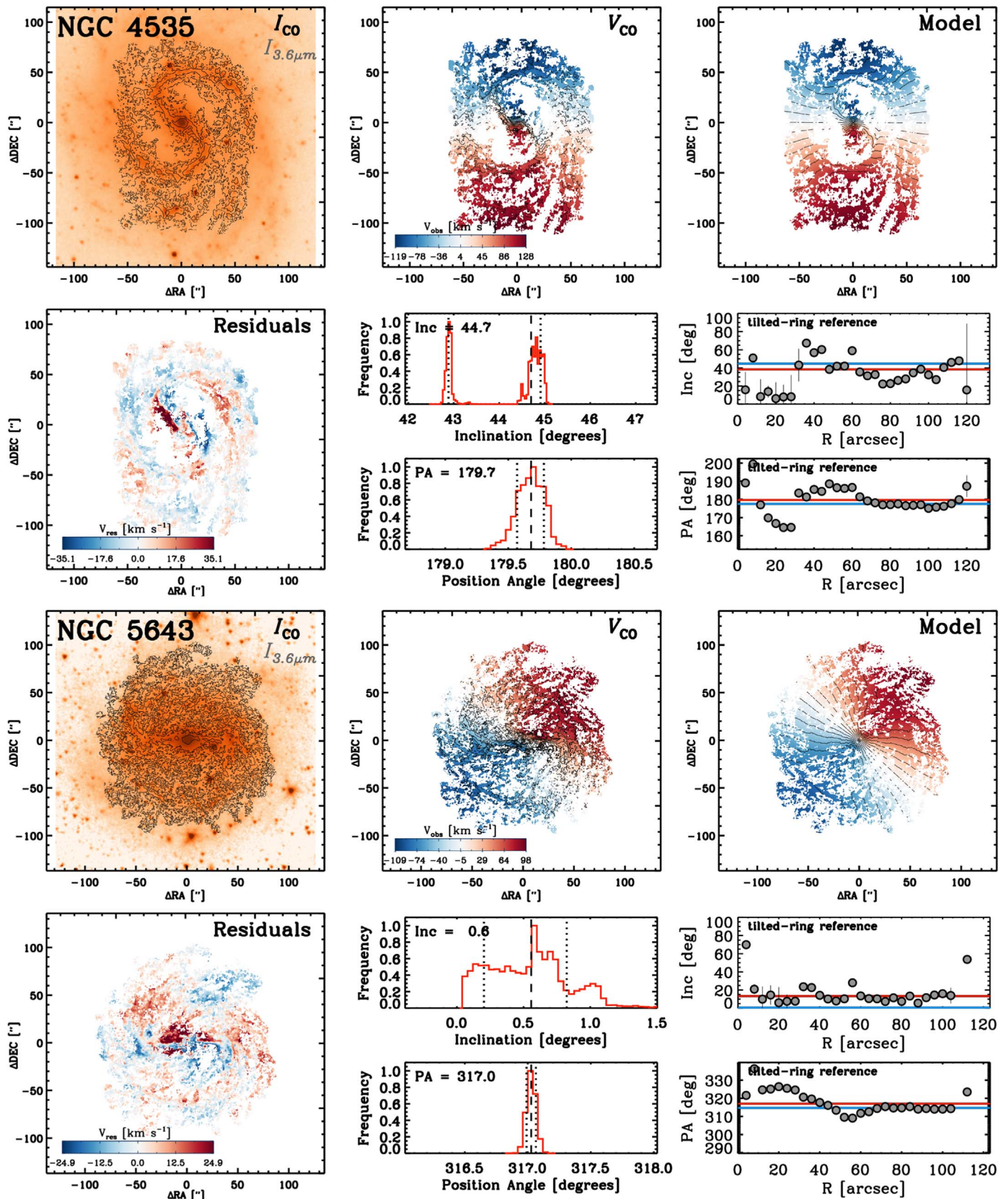


Figure B2. Same as Figure 4, but showing two additional example galaxies to highlight the effect of stellar bars on our kinematic fit performance.

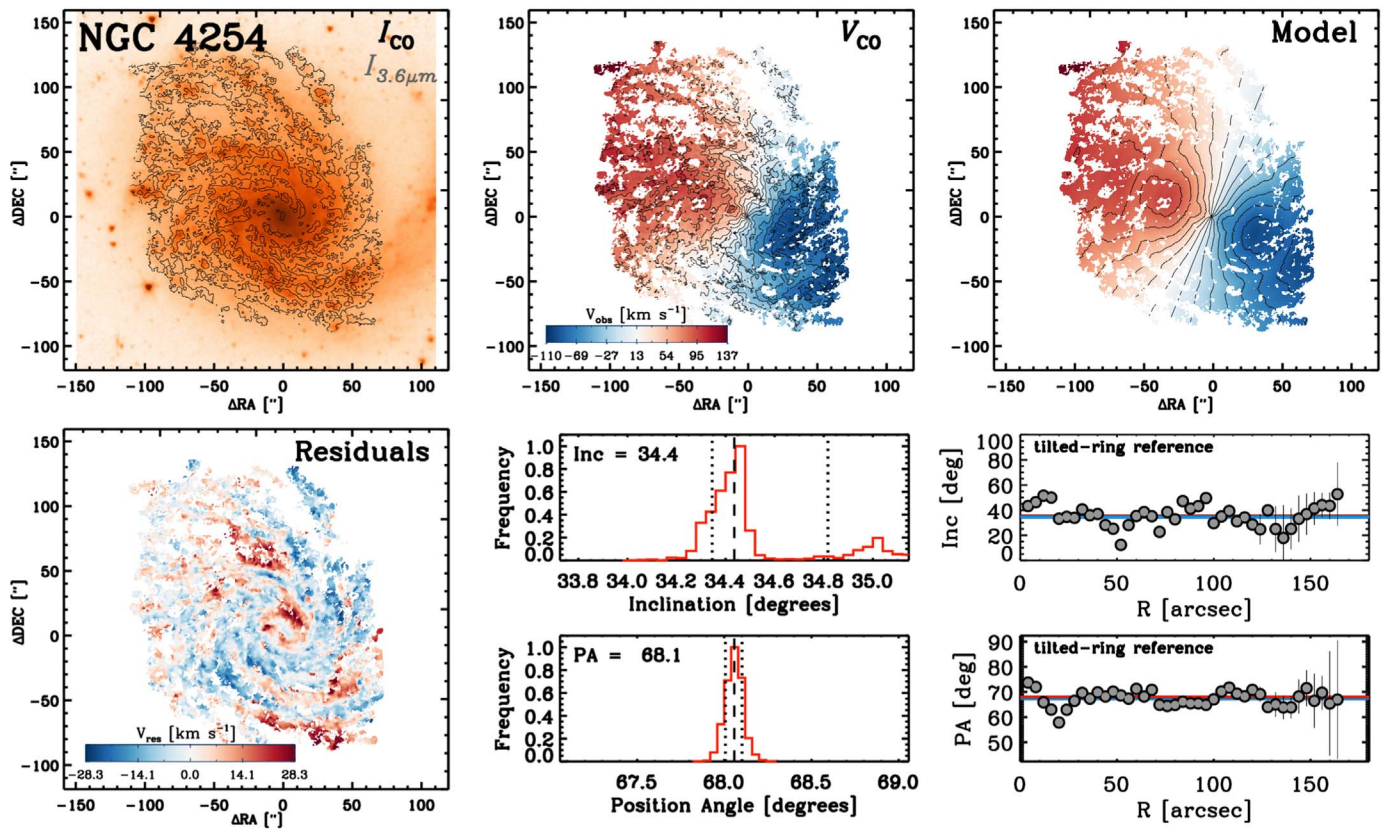


Figure B3. Same as Figure 4, but showing one additional example galaxy to highlight successful fit performance.

Appendix C Orientations Based on 7 m Fits

Table C1 lists the kinematic position angles and inclination angles derived by applying our fitting technique to the PHANGS 7 m velocity fields for our sample of galaxies, as described in Section 4.3.2.

Table C1
Orientation Parameters Based on Fits to the 7 m PHANGS–ALMA CO Maps

ID	ϕ (deg)	i (deg)
IC 1954	52.9	62.9
IC 5273	49.0	231.8
NGC 0628	...	21.4
NGC 0685	35.0	101.1
NGC 1087	32.4	−1.3
NGC 1097	...	127.4
NGC 1300	...	275.0
NGC 1317	...	210.6
NGC 1365	...	202.0
NGC 1385	41.3	183.5
NGC 1433	...	198.8
NGC 1511	...	293.7
NGC 1512	...	263.5
NGC 1546	66.1	146.5
NGC 1559	52.7	245.9
NGC 1566	27.1	215.5
NGC 1672	...	128.2
NGC 1792	58.2	318.4
NGC 1809	72.2	139.6
NGC 2090	65.4	192.4
NGC 2283	34.4	−4.0
NGC 2566	...	312.5
NGC 2775	42.3	157.1
NGC 2835	46.0	0.5
NGC 2903	63.0	204.0
NGC 2997	32.8	107.5
NGC 3059	...	−13.0
NGC 3137	70.3	0.1
NGC 3351	...	192.8
NGC 3507	7.8	57.0
NGC 3511	70.3	257.4
NGC 3521	67.4	343.3
NGC 3596	...	78.0

Table C1
(Continued)

ID	ϕ (deg)	i (deg)
NGC 3621	63.7	343.7
NGC 3626	...	162.6
NGC 3627	53.8	171.1
NGC 4207	...	119.2
NGC 4254	25.1	68.6
NGC 4293	...	63.6
NGC 4298	55.8	313.7
NGC 4303	...	314.4
NGC 4321	30.3	155.0
NGC 4457	...	76.8
NGC 4496	30.2	50.6
NGC 4535	44.8	179.2
NGC 4536	65.9	304.1
NGC 4540	40.5	19.0
NGC 4548	...	136.5
NGC 4569	...	17.6
NGC 4571	27.7	217.2
NGC 4579	40.2	89.9
NGC 4654	57.1	123.3
NGC 4689	37.5	163.9
NGC 4781	55.2	289.7
NGC 4826	46.9	294.6
NGC 4941	46.6	203.1
NGC 4951	65.0	91.1
NGC 5042	48.5	191.8
NGC 5068	...	339.3
NGC 5134	...	319.2
NGC 5248	37.2	108.2
NGC 5530	57.0	306.3
NGC 5643	...	315.8
NGC 6300	51.1	107.5
NGC 6744	51.5	14.1
NGC 7456	51.7	15.6
NGC 7496	29.8	191.0

Appendix D Rotation Curves and Smooth Fits for the Full Sample

Here we present rotation curves for our full set of 67 galaxies (see Figures D1–D4 and Table D1), as shown earlier for 6 galaxies in Figure 7 in the main text.

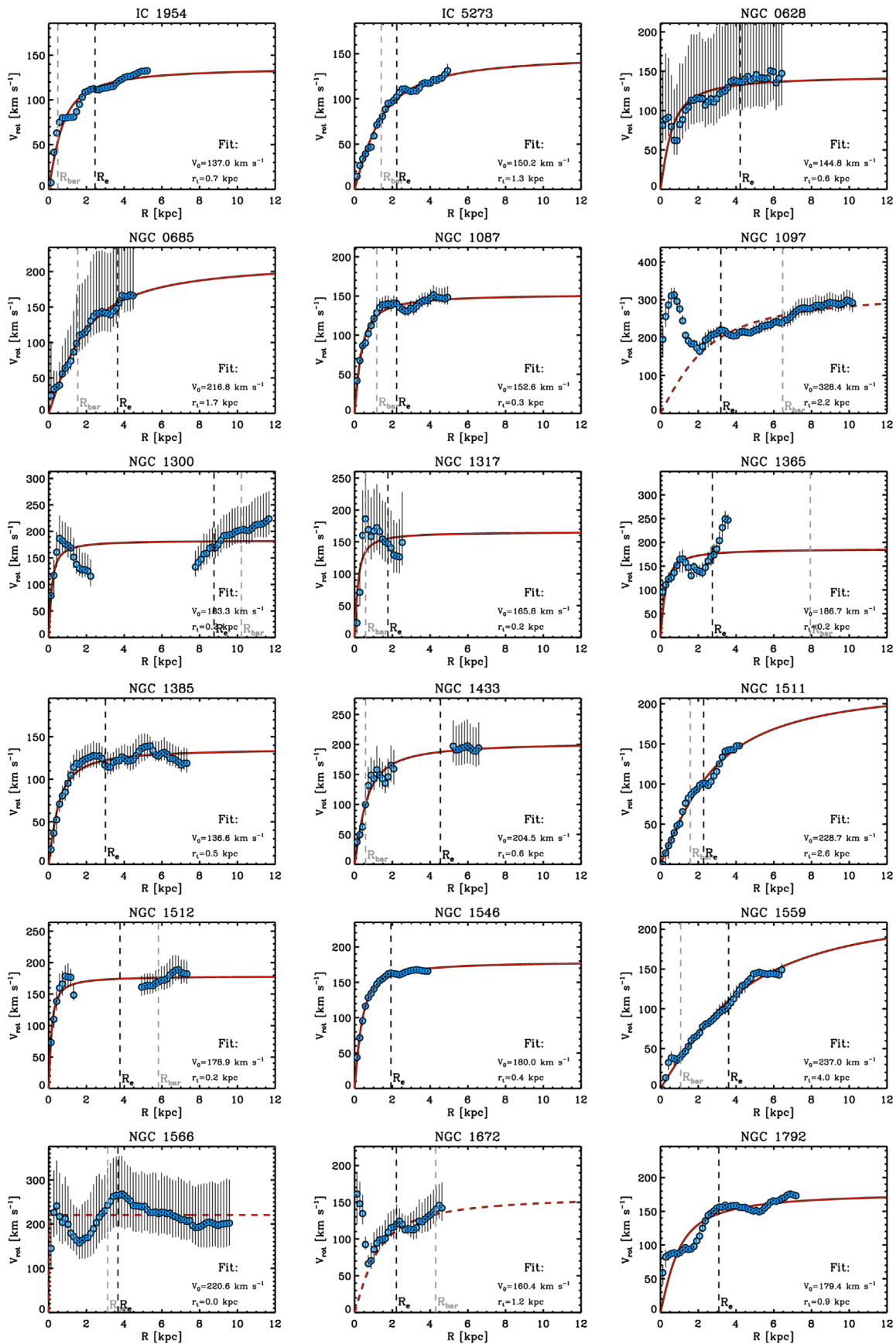


Figure D1. Same as Figure 7, but showing the full galaxy sample.

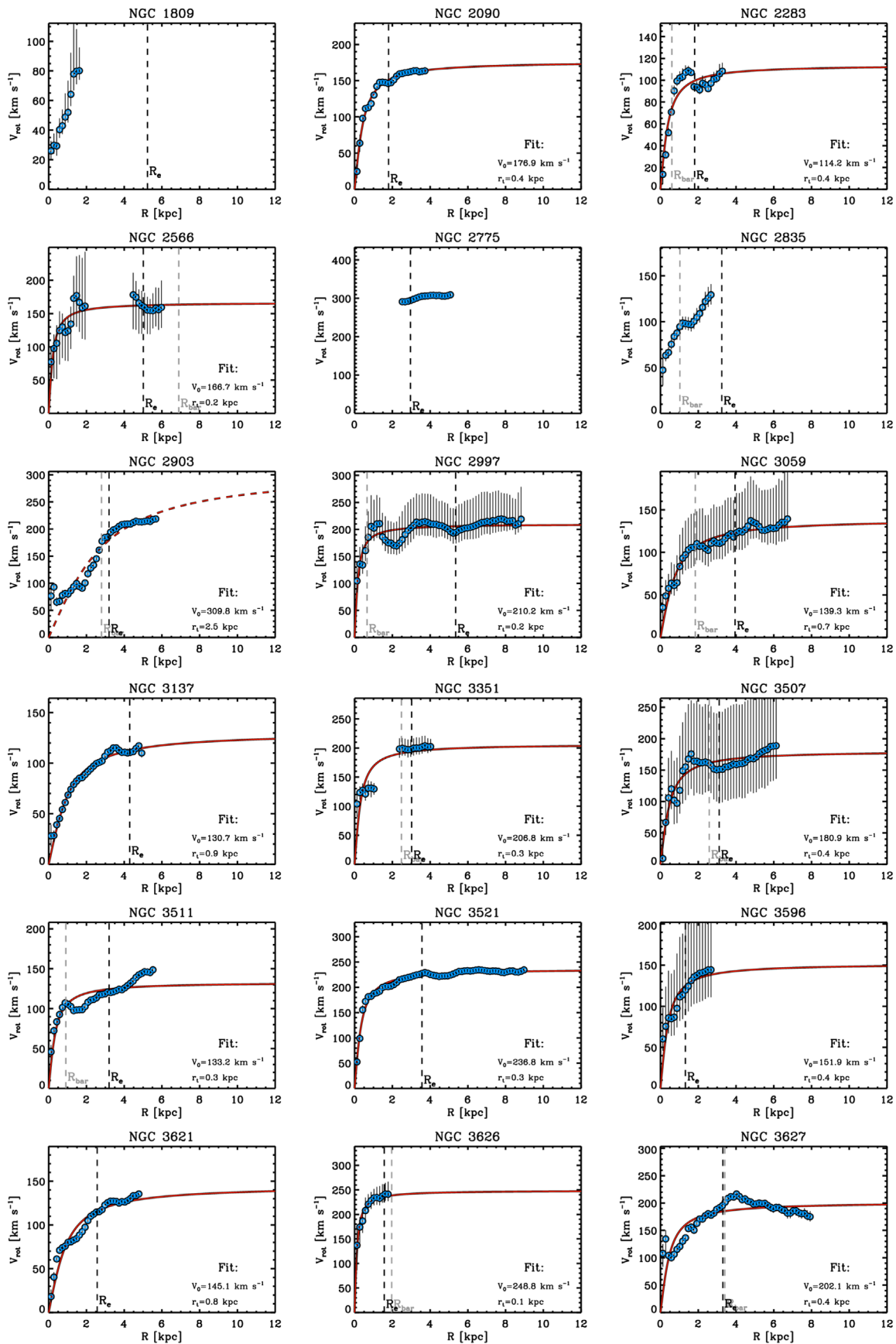


Figure D2. Same as Figure 7, but showing the full galaxy sample.

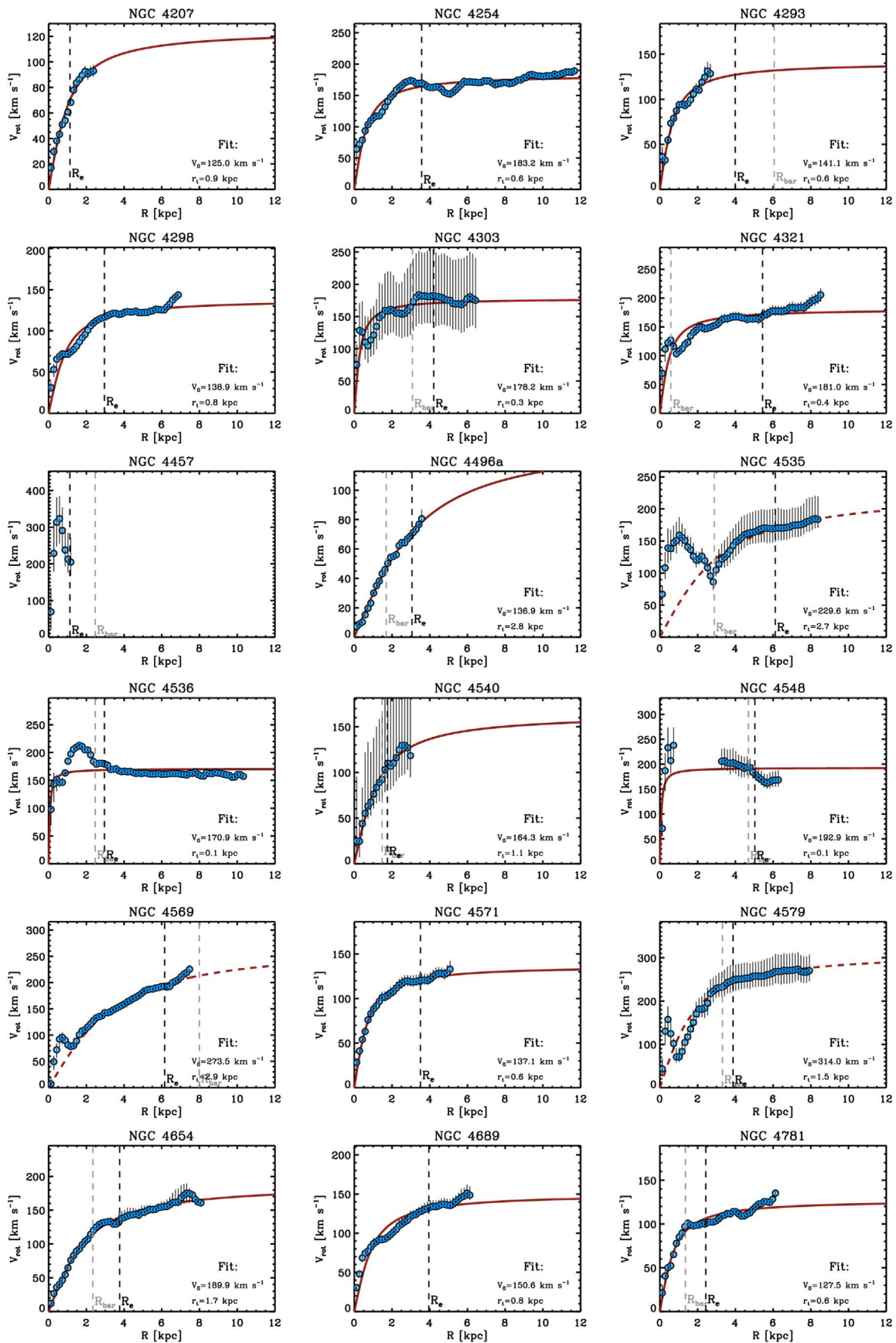


Figure D3. Same as Figure 7, but showing the full galaxy sample.

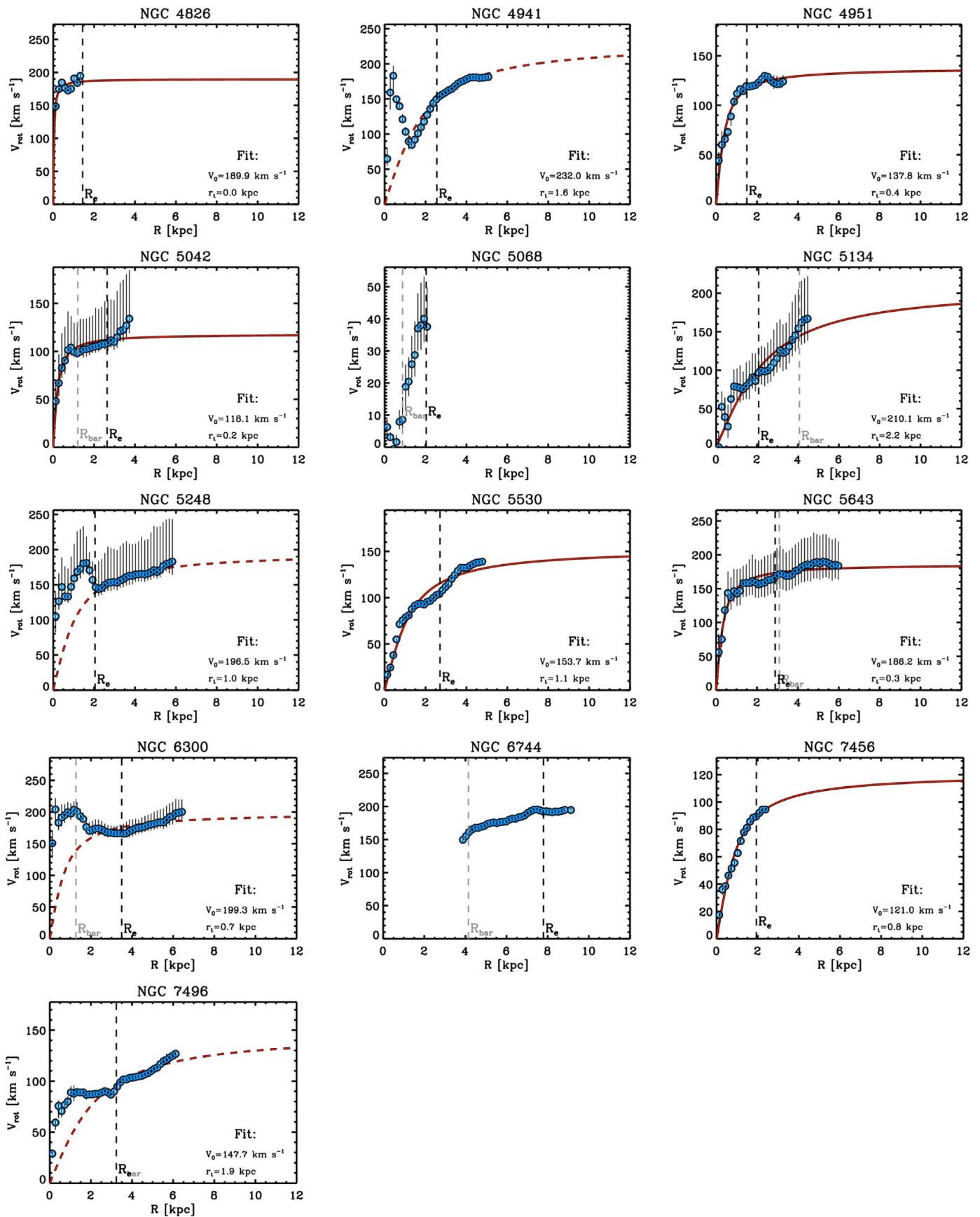


Figure D4. Same as Figure 7, but showing the full galaxy sample

Table D1
Tabulated Rotation Curves for the Full Sample of 67 Galaxies

R (kpc)	Galaxy	V_{rot}^a (km s $^{-1}$)	$V_{\text{rot,err}+}^b$ (km s $^{-1}$)	$V_{\text{rot,err}-}^c$ (km s $^{-1}$)
0.125	IC 1954	7.4	5.0	5.8
0.275	IC 1954	41.3	2.6	7.1
...				
5.075	IC 1954	132.0	4.9	8.9
5.225	IC 1954	123.5	4.0	7.5
...				
0.125	NGC 7496	28.9	4.3	4.6
0.275	NGC 7496	59.4	3.9	7.1
...				
5.975	NGC 7496	124.9	5.0	4.3
6.125	NGC 7496	126.8	3.9	4.9

Notes.^a Rotation velocity V_{rot} per radial bin.^b Upper velocity error.^c Lower velocity error. Velocity errors are based on the 16th and 84th percentiles of the 100 rotation curve realizations (see Section 3.3.2 for details).

(This table is available in its entirety in machine-readable form.)

ORCID iDs

Philipp Lang  <https://orcid.org/0000-0002-5681-3575>
 Sharon E. Meidt  <https://orcid.org/0000-0002-6118-4048>
 Erik Rosolowsky  <https://orcid.org/0000-0002-5204-2259>
 Eva Schinnerer  <https://orcid.org/0000-0002-3933-7677>
 Adam K. Leroy  <https://orcid.org/0000-0002-2545-1700>
 Eric Emsellem  <https://orcid.org/0000-0002-6155-7166>
 Brent Groves  <https://orcid.org/0000-0002-9768-0246>
 Annie Hughes  <https://orcid.org/0000-0002-9181-1161>
 Frank Bigiel  <https://orcid.org/0000-0003-0166-9745>
 Christopher Faesi  <https://orcid.org/0000-0001-5310-467X>
 Daizhong Liu  <https://orcid.org/0000-0001-9773-7479>
 Jérôme Pety  <https://orcid.org/0000-0003-3061-6546>
 Toshiki Saito  <https://orcid.org/0000-0002-2501-9328>
 Jiayi Sun  <https://orcid.org/0000-0003-0378-4667>
 Antonio Usero  <https://orcid.org/0000-0003-1242-505X>

References

- Begeman, K. G. 1987, PhD thesis, Kapteyn Institute
 Bluck, A. F. L., Mendel, J. T., Ellison, S. L., et al. 2014, *MNRAS*, **441**, 599
 Boizelle, B. D., Barth, A. J., Walsh, J. L., et al. 2019, *ApJ*, **881**, 10
 Boone, F., Baker, A. J., Schinnerer, E., et al. 2007, *A&A*, **471**, 113
 Bosma, A. 1978, PhD thesis, Groningen Univ.
 Bouche, N., Carfantan, H., Schroetter, I., Michel-Dansac, L., & Contini, T. 2015, *AJ*, **150**, 92
 Briggs, F. H. 1990, *ApJ*, **352**, 15
 Canzian, B. 1993, *ApJ*, **414**, 487
 Casoli, F., & Gerin, M. 1993, *A&A*, **279**, 41
 Chemin, L., Huré, J.-M., Soubiran, C., et al. 2016, *A&A*, **588**, A48
 Chemin, L., Renaud, F., & Soubiran, C. 2015, *A&A*, **578**, A14
 Chevance, M., Kruijssen, J. M. D., Hygate, A. P. S., et al. 2020, *MNRAS*, **493**, 2872
 Chung, A., van Gorkom, J. H., Kenney, J. D. P., et al. 2009, *AJ*, **138**, 1741
 Colombo, D., Meidt, S. E., Schinnerer, E., et al. 2014, *ApJ*, **784**, 4
 Combes, F., & Becquaert, J.-F. 1997, *A&A*, **326**, 554
 Courteau, S. 1997, *AJ*, **114**, 2402
 Davis, T. A., Bureau, M., Onishi, K., et al. 2018, *MNRAS*, **473**, 3818
 Davis, T. A., & McDermid, R. M. 2017, *MNRAS*, **464**, 453
 de Blok, W. J. G., Walter, F., Brinks, E., et al. 2008, *AJ*, **136**, 2648
 di Teodoro, E. M., & Fraternali, F. 2015, *MNRAS*, **451**, 3021
 Dobbs, C. L., & Pringle, J. E. 2009, *MNRAS*, **396**, 1579
 Dutton, A. A., & van den Bosch, F. C. 2009, *MNRAS*, **396**, 141
 Epinat, B., Amram, P., Marcelin, M., et al. 2008, *MNRAS*, **388**, 500
 Fathi, K., van de Ven, G., Peletier, R. F., et al. 2005, *MNRAS*, **364**, 773
 Foreman-Mackey, D., Hogg, D. W., Lang, D., et al. 2013, *PASP*, **125**, 306
 Franx, M., van Gorkom, J. H., & de Zeeuw, P. T. 1994, *ApJ*, **436**, 642
 Freeman, P., Rosolowsky, E., Kruijssen, J. M. D., et al. 2017, *MNRAS*, **468**, 1769
 Helfer, T. T., Thornley, M. D., Regan, M. W., et al. 2003, *ApJS*, **145**, 259
 Henshaw, J. D., Kruijssen, J. M. D., Longmore, S. N., et al. 2020, *NatAs*, submitted
 Herrera, C. N., Pety, J., Hughes, A., et al. 2020, *A&A*, **634**, A121
 Herrera-Endoqui, M., Díaz-García, S., Laurikainen, E., et al. 2015, *A&A*, **582**, A86
 Hunt, L. K., Combes, F., & García-Burillo, S. 2008, *A&A*, **482**, 133
 Jarrett, T. H., Chester, T., Cutri, R., et al. 2003, *AJ*, **125**, 52
 Jogee, S., Barazza, F. D., Rix, H.-W., et al. 2004, *ApJL*, **615**, 108
 Józsa, G. I. G., Kenn, F., Klein, U., & Oosterloo, T. A. 2007, *A&A*, **468**, 731
 Kalinova, V., van de Ven, G., Lyubenova, M., et al. 2017, *MNRAS*, **464**, 1903
 Kamphuis, P., Józsa, G. I. G., Oh, S.-H., et al. 2015, *MNRAS*, **452**, 3139
 Kim, W.-T., & Ostriker, E. C. 2006, *ApJ*, **646**, 213
 Kormendy, J., & Kennicutt, R. C. 2004, *ARA&A*, **42**, 603
 Korsaga, M., Carignan, C., Amram, P., et al. 2018, *MNRAS*, **478**, 50
 Krajnović, D., Cappellari, M., de Zeeuw, P. T., & Copin, Y. 2006, *MNRAS*, **366**, 787
 Kruijssen, J. M. D., Dale, J. E., Longmore, S. N., et al. 2019, *MNRAS*, **484**, 5734
 Lelli, F., McGaugh, S. S., & Schombert, J. M. 2016, *AJ*, **152**, 157
 Leroy, A. K., Sandstrom, K. M., Lang, D., et al. 2019, *ApJS*, **244**, 24
 Leroy, A. K., Schinnerer, E., Hughes, A., et al. 2017, *ApJ*, **846**, 71
 Leung, G. Y. C., Leaman, R., van de Ven, G., et al. 2018, *MNRAS*, **477**, 254
 Levy, R. C., Bolatto, A. D., Sánchez, S. F., et al. 2019, *ApJ*, **882**, 84
 Levy, R. C., Bolatto, A. D., Teuben, P., et al. 2018, *ApJ*, **860**, 92
 Makarov, D., Prugniel, P., Terekhova, N., Courtois, H., & Vaughlin, I. 2014, *A&A*, **570**, A13
 McGaugh, S. S., & Schombert, J. M. 2015, *ApJ*, **802**, 18
 Meidt, S. E., Leroy, A. K., Rosolowsky, E., et al. 2018, *ApJ*, **854**, 100
 Meidt, S. E., Schinnerer, E., García-Burillo, S., et al. 2013, *ApJ*, **779**, 45
 Muñoz-Mateos, J. C., Sheth, K., Gil de Paz, A., et al. 2013, *ApJ*, **771**, 59
 Oh, S.-H., Staveley-Smith, L., Spekkens, K., et al. 2018, *MNRAS*, **473**, 3256
 Onishi, K., Iguchi, S., Davis, T. A., et al. 2017, *MNRAS*, **468**, 4663
 Paturel, G., Petit, C., Prugniel, P., et al. 2003, *A&A*, **412**, 45
 Peters, S. P. C., van der Kruit, P. C., Allen, R. J., & Freeman, K. C. 2017, *MNRAS*, **464**, 21
 Ponomareva, A. A., Verheijen, M. A. W., & Bosma, A. 2016, *MNRAS*, **463**, 4052
 Puschign, J., Hayes, M., Östlin, G., et al. 2020, arXiv:2004.09142
 Querejeta, M., Meidt, S. E., Schinnerer, E., et al. 2015, *ApJS*, **219**, 5
 Roberts, W. W., & Stewart, G. R. 1987, *ApJ*, **314**, 10
 Rogstad, D. H., Lockhart, I. A., & Wright, M. C. H. 1974, *ApJ*, **193**, 309
 Salo, H., Laurikainen, E., Laine, J., et al. 2015, *ApJS*, **219**, 4
 Schinnerer, E., Meidt, S. E., Pety, J., et al. 2013, *ApJ*, **779**, 42
 Schmidt, T. M., Bigiel, F., Klessen, R. S., et al. 2016, *MNRAS*, **457**, 2642
 Schoenmakers, R. H. M. 1999, PhD thesis, Univ. Groningen
 Schoenmakers, R. H. M., Franx, M., & de Zeeuw, P. T. 1997, *MNRAS*, **292**, 349
 Schruha, A., Leroy, A. K., Walter, F., et al. 2011, *AJ*, **142**, 37
 Sellwood, J. A. 2010, in *Planets, Stars and Stellar Systems*, ed. T. D. Oswalt & G. Gilmore, Vol. 5 (Berlin: Springer)
 Sellwood, J. A., & Sánchez, R. Z. 2010, *MNRAS*, **404**, 1733
 Sheth, K., Regan, M., Hinz, J. L., et al. 2010, *PASP*, **122**, 1397
 Simon, J. D., Bolatto, A. D., Leroy, A., & Blitz, L. 2003, *ApJ*, **596**, 957
 Sofue, Y., & Rubin, V. 2001, *ARA&A*, **39**, 137
 Sormani, M., Binney, J., & Magorrian, J. 2015, *MNRAS*, **449**, 2421
 Spekkens, K., & Sellwood, J. A. 2007, *ApJ*, **664**, 204
 Sun, J., Leroy, A. K., Schruha, A., et al. 2018, *ApJ*, **860**, 172
 Trachternach, C., de Blok, W. J. G., Walter, F., et al. 2008, *AJ*, **136**, 2720
 Tully, R. B., & Fisher, J. R. 1977, *A&A*, **54**, 661
 Tully, R. B., Rizzi, L., Shaya, E. J., et al. 2009, *AJ*, **138**, 323
 Van Albada, T. S., Bahcall, J. N., Begeman, K., & Sancisi, R. 1985, *ApJ*, **295**, 305
 van de Ven, G., & Fathi, K. 2010, *ApJ*, **723**, 767
 van der Hulst, J. M., Terlouw, J. P., Begeman, K. G., Zwitser, W., & Roelfsema, P. R. 1992, in *ASP Conf. Ser. 25, Astronomical Data Analysis Software and Systems I*, ed. D. M. Worrall, C. Biemesderfer, & J. Barnes (San Francisco: ASP), **131**
 van der Wel, A., Chang, Y.-Y., Bell, E. F., et al. 2014, *ApJL*, **792**, L6
 Wong, T., Blitz, L., & Bosma, A. 2004, *ApJ*, **605**, 183
 Yoachim, P., & Dalcanton, J. J. 2006, *AJ*, **131**, 226
 Yoshino, A., & Ichikawa, T. 2008, *PASJ*, **60**, 493